Journal of Structural Geology 101 (2017) 58–79

Contents lists available at ScienceDirect

Journal of Structural Geology

journal homepage: www.elsevier.com/locate/jsg

Fluids along the North Anatolian Fault, Niksar basin, north central Turkey: Insight from stable isotopic and geochemical analysis of calcite veins

Colin P. Sturrock [a], Elizabeth J. Catlos [b, *], Nathan R. Miller [b], Aykut Akgun [c], András Fall [d], Rinat I. Gabitov [e], Ismail Omer Yilmaz [f], Toti Larson [b], Karen N. Black [g]

[a] University of Colorado, Dept. of Geological Sciences, UCB 399, Boulder, CO, 80309-0399, USA
[b] The University of Texas at Austin, Jackson School of Geosciences, Dept. of Geological Sciences, 1 University Sta. C9000, EPS 1.130, Austin, TX, 78712, USA
[c] Karadeniz Technical University, Geological Engineering Department, Applied Geology Division, Trabzon, Turkey
[d] The University of Texas at Austin, Jackson School of Geosciences, Bureau of Economic Geology, University Station Box X, Austin, TX 78713-8924, USA
[e] Mississippi State University, Department of Geosciences, 108 Hilbun Hall, P.O. Box 5448, MS, 39762-5448, USA
[f] Middle East Technical University, Geological Engineering Department, 06800, Ankara, Turkey
[g] Core Laboratories, 6316 Windfern Rd., Houston, TX, 77040, USA

ARTICLE INFO

Article history:
Received 29 September 2016
Received in revised form
22 May 2017
Accepted 7 June 2017
Available online 10 June 2017

Keywords:
Tectonic veins
Stable isotopes
North Anatolian Fault
Trace elements
Fluid flow
Fractures

ABSTRACT

Six limestone assemblages along the North Anatolian Fault (NAF) Niksar pull-apart basin in northern Turkey were analyzed for $\delta^{18}O_{PDB}$ and $\delta^{13}C_{PDB}$ using bulk isotope ratio mass spectrometry (IRMS). Matrix-vein differences in $\delta^{18}O_{PDB}$ (−2.1 to 6.3‰) and $\delta^{13}C_{PDB}$ (−0.9 to 4.6‰) suggest a closed fluid system and rock buffering. Veins in one travertine and two limestone assemblages were further subjected to cathodoluminescence, trace element (Laser Ablation Inductively Coupled Plasma Mass Spectrometry) and $\delta^{18}O_{PDB}$ (Secondary Ion Mass Spectrometry, SIMS) analyses. Fluid inclusions in one limestone sample yield T_h of 83.8 ± 7.3 °C (±1σ, mean average). SIMS $\delta^{18}O_{PDB}$ values across veins show fine-scale variations interpreted as evolving thermal conditions during growth and limited rock buffering seen at a higher-resolution than IRMS. Rare earth element data suggest calcite veins precipitated from seawater, whereas the travertine has a hydrothermal source. The $\delta^{18}O_{SMOW\text{-}fluid}$ for the mineralizing fluid that reproduces T_h is +2‰, in range of Cretaceous brines, as opposed to negative $\delta^{18}O_{SMOW\text{-}fluid}$ from meteoric, groundwater, and geothermal sites in the region and highly positive $\delta^{18}O_{SMOW\text{-}fluid}$ expected for mantle-derived fluids. Calcite veins at this location do not record evidence for deeply-sourced metamorphic and magmatic fluids, an observation that differs from what is reported for the NAF elsewhere along strike.

1. Introduction

Fluid pressure has a significant effect on earthquake rupturing and fault slip behavior (e.g., Sibson et al., 1975; Bredehoeft and Ingebritsen, 1990; Rice, 1992; Byerlee, 1993; Sibson, 1996; Chiodini et al., 2004; Miller et al., 2004; De Leeuw et al., 2010). Increased permeability as a direct result of faulting is assumed in many of these cases, but fracture networks can also form impermeable barriers or combined permeable and impermeable zones (e.g., Caine et al., 1996; Frima et al., 2005; Olierook et al., 2014; Ran et al., 2014). Passive and dynamic open-mode fracturing occurs in transtensional settings, each having differing implications for the nature of fluids recorded in rock fractures (e.g. Sample, 2010; Uysal et al., 2011; Nuriel et al., 2012a, 2012b). Dynamic fractures open episodically due to seismic events, and fluids are mobilized to form veins (e.g., Hilgers and Urai, 2002; Nuriel et al., 2012a). Vein mineralization in passive fractures may occur over short timescales after earthquake activity, with distinct episodes of mineral deposition mediated via the influx of fluids (Moore et al., 2000). Thus veins have the potential to directly record information regarding fluid composition and the permeability of fracture networks after seismic activity (Verhaert et al., 2003, 2004).

Here we seek to understand the nature, source, and extent of

* Corresponding author.
E-mail address: ejcatlos@gmail.com (E.J. Catlos).

http://dx.doi.org/10.1016/j.jsg.2017.06.004
0191-8141/

fluids recorded by fracture networks along the seismically-active North Anatolian Fault (NAF) in north central Turkey, in portions of the fault system that displace Upper Jurassic to Lower Cretaceous carbonate assemblages at the surface (Fig. 1). Geochemical signatures for deep crustal- or mantle-derived fluids may exist within fault rock calcite veins, and such evidence would indicate that NAF deformation results in vertically permeable fracture networks accessing deep, over-pressured fluids (e.g., Pili et al., 2002, 2011). Alternatively, diagenetic processes may dominate, and calcite veins record only precipitation or mineralization during previous events related to the closure of the Tethyan oceans with no evidence of more recent activity. Discerning the processes responsible for the formation of calcite veins in rocks displaced by the NAF is possible by employing multiple geochemical and isotopic tracers.

Geochemical evidence for fluid sources tapped by NAF fracture systems potentially exists within calcite veins in limestone rocks collected directly from fault planes or fault-related fractures (e.g., Janssen et al., 1997, 2009; De Leeuw et al., 2010; Crémiére et al., 2012). The rocks displaced by the NAF have experienced a multi-stage history, thus discriminating veins that result from mineral precipitation due to pressure changes and fluid unmixing after earthquake rupture (e.g., Uysal et al., 2011) from those associated with diagenesis (e.g., Morad et al., 2010) or previous metamorphic cycles associated with the closure of Tethyan oceans (e.g., Bektaş et al., 2001; Yilmaz, 2006) remains unknown. In strike slip systems and within the NAF, the extent of vertical fluid flow in fault zones is unclear as a number of controls influence migration (e.g., Peacock and Anderson, 2012; Ritz et al., 2015). The results reported here have implications for understanding the nature of regional-scale fluid-flow within the NAF and the use of isotopic data from calcite veins as recorders of seismic activity (Roberts, 1994; Uysal et al., 2011; Dabi et al., 2013).

Ample evidence exists for deep crustal and magmatic fluid migrating vertically through the NAF and related deformation zones at specific locations along strike. For example, contributions of mantle helium in hydrothermal fluids from areas along the NAF associated with seismic activity have increased after seismic events (Doğan et al., 2009; De Leeuw et al., 2010; Burnard et al., 2012). Magnetotelluric studies show increased conductivity in deformed crust beneath the NAF trace (Türkoğlu et al., 2015), and seismic tomography indicates a pervasive low-velocity zone that extends into the mantle, interpreted to be a zone of deformation associated with the NAF (Fichtner et al., 2013). Clay minerals from NAF planes have $\delta^{18}O$ and δD values consistent with deeply sourced metamorphic and magmatic fluids that have migrated as a result of fault activity (Uysal et al., 2006).

This study is the first to present $\delta^{18}O_{PDB}$ Secondary Ion Mass Spectrometry (SIMS) data from NAF calcite veins, which shows promise for deciphering small-scale variations in larger veins and discriminating among different smaller fracture generations (Sample, 2010). The results are further informed by bulk isotope ratio mass spectrometry (IRMS), fluid inclusion analyses, cathodoluminescence (CL) images, and petrography. The data provide insight regarding changes in fluid source and temperature, and are used to infer chemical processes occurring during crystallization.

2. Geologic background

The North Anatolian Fault (NAF) (Fig. 1) is a 1200 km-long dextral strike-slip fault which extends from the town of Karliova in northeastern Turkey, paralleling the coast of the Black Sea, across the Northern Aegean Sea, central and mainland Greece, eventually linking with the Hellenic subduction zone (e.g. Barka, 1992; Barka, 1996; Barka et al., 2000; Şengör et al., 2005). The structure is part of a larger zone of deformation called the North Anatolian Shear Zone (NASZ) (Şengör et al., 1985, 2005), which lies along the boundary between the Eurasian plate to the north and the Anatolian microplate to the south. Its dextral slip accommodates the counterclockwise rotation and westward escape due to the collision between the Arabian and Anatolian plates (Barka and Hancock, 1984; Piper et al., 2010).

The focus of this study is the Erbaa-Niksar basin in the Tokat Massif of NE Turkey. The basin is considered one of the widest (12–13 km) active pull-apart basins along the NAF (Figs. 1 and 2) (Barka et al., 2000; Ozden et al., 2002; Bektaş et al., 2001). The strike of the NAF between the towns of Erzincan and Erbaa is approximately 105°, whereas adjacent segments are 120°-125° (Fig. 1). A zone of convergent, N-S directed, E-W trending strain intersects with ideal strike-slip motion on the eastern part of the NAF, and is responsible for the origin of the Erbaa-Niksar basin (Şengör et al., 1985). It is Z-shaped, bounded to the north by the Niksar-Kaleköy fault segment which ruptured in 1942 (Ms = 7.1) and 1943 (Ms = 7.4) and to the south by the Erzincan or Ezine Pazarı fault which ruptured in 1939 (Ms 7.8) (e.g., Mann et al., 1983; Ambraseys and Jackson, 1998; Tatar et al., 2007; Gürsoy et al., 2013; Demir et al., 2015). The southern boundary is part of a series of faults at a major NAF step over (Barka et al., 2000; Zabci et al., 2011). The Erbaa-Niksar basin has been a key component used to model NAF evolution and slip history (Barka and Hancock, 1984; Tatar et al., 1995; Barka et al., 2000; Gokten et al., 2013), and is also termed separately Niksar and Erbaa-Taşova (e.g., Hempton and Dunne, 1984; Barka et al., 2000).

Mammal fossils from the Erbaa-Taşova portion of the basin place a minimum age for its formation in Early Pliocene, with initiation of the fault zone in this area in Late Miocene to Early Pliocene (Barka et al., 2000; Erol and Topal, 2013). Assuming that Erbaa-Taşova basin length and total fault displacement are directly related suggests a total displacement of 65 km for this part of the NAF. The Niksar basin (Fig. 2) is shorter in length (~15 km), and thus accommodates less displacement, making its age 0.5–1 Ma when extrapolating from slip rate estimates of 15–20 mm/yr (Barka et al., 2000; Hubert-Ferrari et al., 2002). Sedimentary units comprising the Niksar basin are younger than the Erbaa-Taşova (primarily Quaternary) and contain evidence of Quaternary volcanism (Adiyaman et al., 2001; Tatar et al., 2007).

Basement rocks of the Erbaa-Niksar basin are part of the Tokat Massif (Rojay, 1995; Yilmaz and Yilmaz, 2004; Catlos et al., 2013) and are separated by regional unconformities (Yilmaz et al., 1997; Yilmaz and Yilmaz, 2004). The basement units are: (1) Triassic metamorphic rocks of the Karakaya accretionary complex, (2) Liassic to Mid-Cretaceous carbonates, clastic sediments and volcanic rocks, (3) Upper Cretaceous limestones, volcanic rocks and ophiolites, and (4) Eocene volcanic and sedimentary rocks (Yilmaz et al., 1997; Yilmaz and Yilmaz, 2004; Erturac and Tüysüz, 2012). These units are exposed along the western boundary of the Niksar basin and along the principal displacement zone along the Erbaa-Taşova basin (Fig. 1) (Barka et al., 2000; Erturac and Tüysüz, 2012).

3. Methods

3.1. Sampling and analytical strategy

Our approach is to apply a combination of bulk (IRMS) and high-resolution (laser ablation inductively coupled plasma mass spectrometry, LA-ICP-MS and SIMS) geochemical tools to six fractured limestone assemblages collected from exposures of the NAF and within the Erbaa-Niksar basin in north-central Turkey (Fig. 1). Calcite matrix (the rock material surrounding the vein) and vein fill were characterized petrologically and analyzed using IRMS for oxygen and carbon ($\delta^{18}O_{PDB}$, $\delta^{13}C_{PDB}$). Based on petrography, IRMS

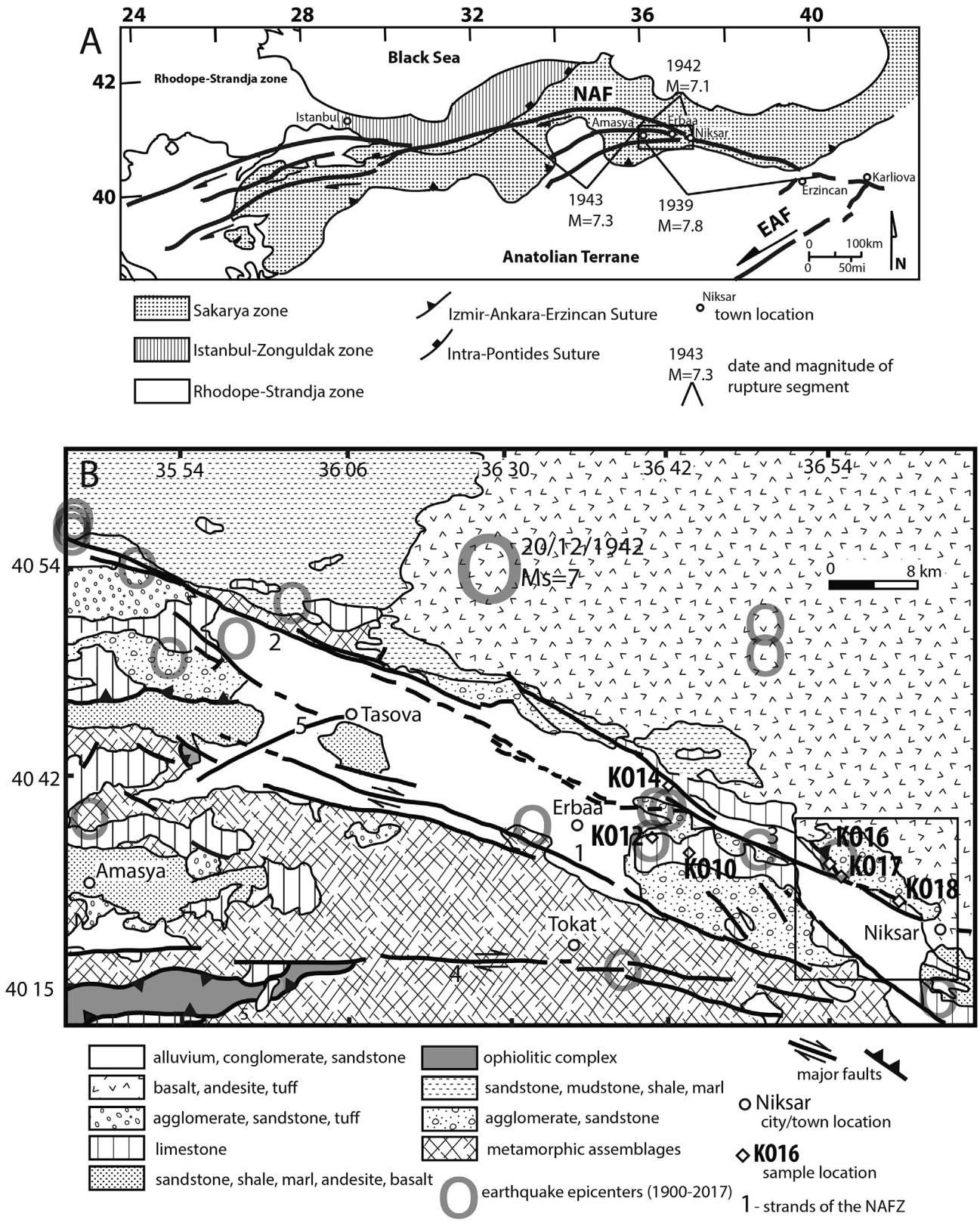

Fig. 1. (A) Geometry and location of the North Anatolian fault zone across Turkey after Barka (1992), (1996) and Akyuz et al. (2002). Sutures and location of the Tethyan terranes after Moix et al. (2008). NAF = North Anatolian Fault; EAF = East Anatolian Fault. Box shows location of the study area (panel B). Also shown are approximate boundaries of rupture from earthquakes (1939, 1942, and 1943) within the field area with magnitudes shown after Şengör et al. (2005). (B) Schematic geologic map showing major basement units in Tokat Massif after Aktimur et al. (1990), Yoshioka (1996), and Barka et al. (2000). Fault strands (names vary) are (1) Erbaa or Esençay, (2) Tosya-Ladik, (3) Niksar-Kaleköy, (4) Erzincan, Ezine Pazarı, or Ezinepazar-Sungurlu (5) Taşova-Tekke (Aktimur et al., 1990; Tatar et al., 1995; Erturac and Tüysüz, 2012; Emre et al., 2012). Strands (2) and (3) are part of the main NAF which ruptured in 1942 and 1943, respectively. Strand (4) ruptured in 1939 (Erturac and Tüysüz, 2012). Sample locations shown. Box indicates the region shown in Fig. 2. Epicenter of earthquakes recorded in the field area from 1900-2017 from data provided by the Republic of Turkey Prime Ministry Disaster and Emergency Management Authority database (http://www.deprem.gov.tr). See Table 3 for details.

data, and location, samples KO16, KO17, and KO18 were selected for further in situ (in thin section or in rock sample) analysis. Rare earth elements (REE), Y, and Mn contents were obtained from polished offcuts of the same in the samples veins using LA-ICP-MS, followed by $\delta^{18}O_{PDB}$ using SIMS. Details of each method and all quantitative data are available as Supplementary files.

Fig. 3 shows the carbonate rock assemblages analyzed in this study. Samples KO14, KO16, KO17, and KO18 were collected directly along the NAF, whereas samples KO10 and KO12 were collected from within the Erbaa-Taşova basin (Figs. 1 and 2). Note that the exact location of the mapped NAF differs depending on field interpretation, thus we provide sample locations in Table 1 and as KML (GoogleMaps) files. Photographs of sample locations of KO16, KO17, and KO18 are shown in Fig. 2. All rocks are fine-grained, massively-bedded, white, pink, grey, or yellow micrites with evidence for extensive brittle deformation and pervasive calcite veins. They are part of the Doğdu Formation, platform carbonate sequences that formed in the Late Jurassic to Early Cretaceous on the southern passive margin of the Neo-Tethys Ocean (Aktimur et al., 1990; Bektaş et al., 2001; Herece and Akay, 2003; Yilmaz, 2006; Cengiz Cinku, 2011). These rocks record regional extensional, rift-related events associated with the break-up of the carbonate platform in the Late Barremian to Early Aptian (e.g., Bektaş et al., 2001; Yilmaz, 2006).

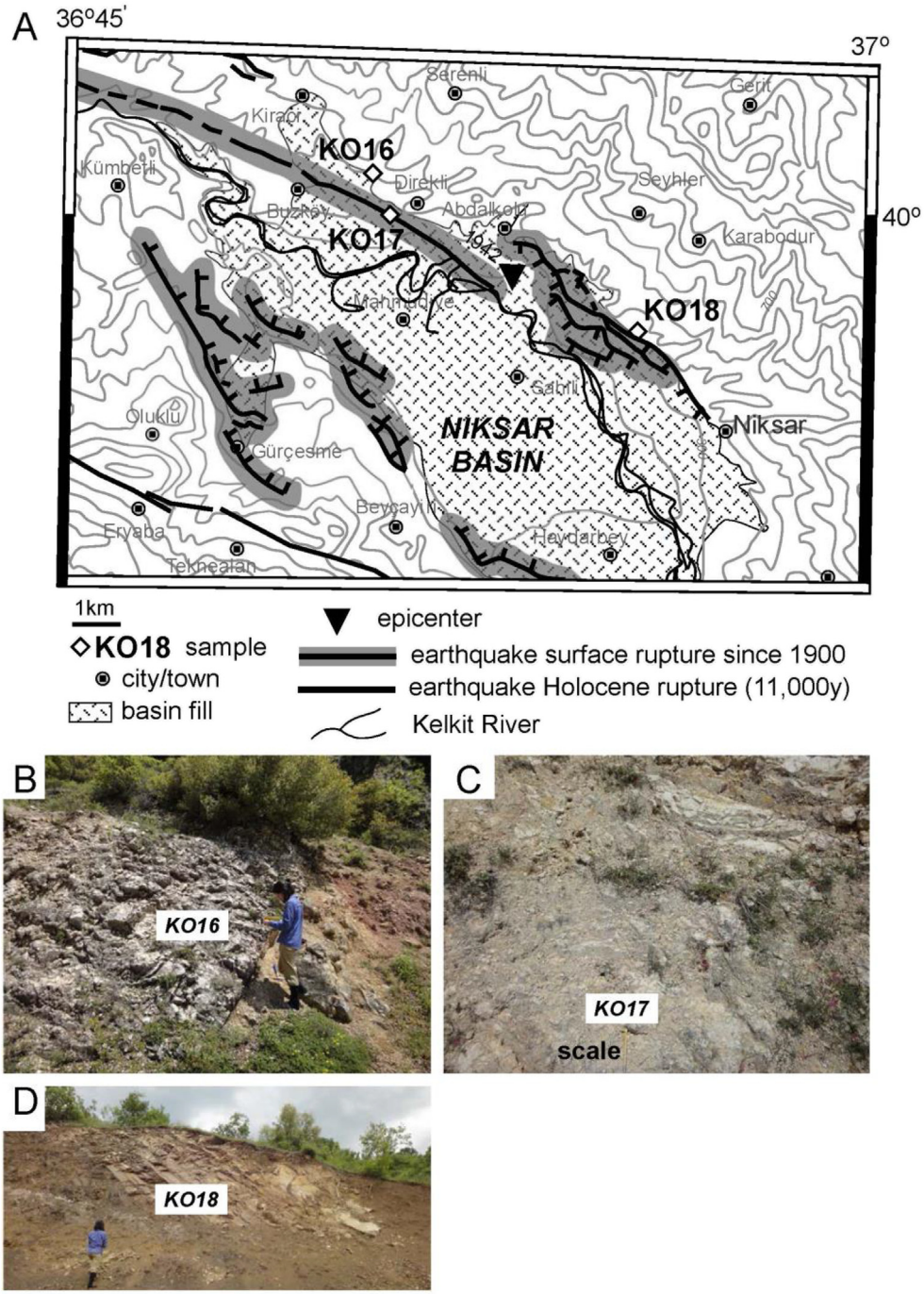

Fig. 2. (A) Active fault map of the Niksar basin after Emre et al. (2012). Sample locations of KO16, KO17, and KO18 are indicated. (B–D) Field photos of these sampling locations.

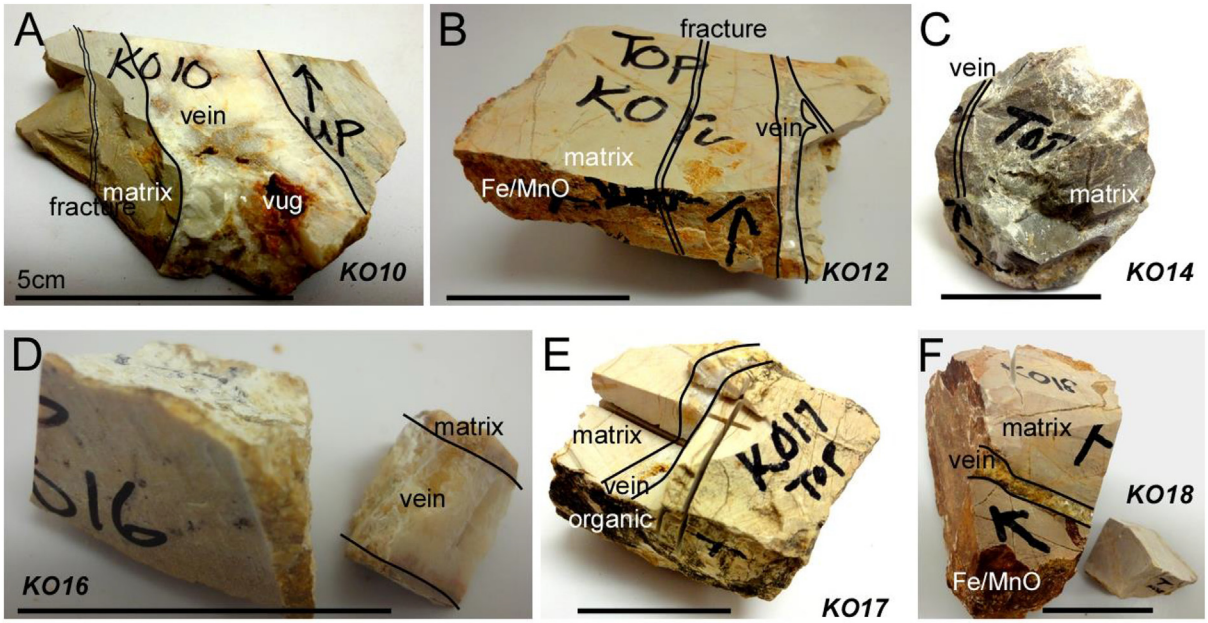

Fig. 3. Hand sample photographs of rocks analyzed in this study. Regions of vein and matrix are indicated on the images. Scale bar is 5 cm.

For each rock, the primary focus was the analysis of calcite veins. All rocks were subjected to standard optical petrography and specific regions were selected for further geochemical analysis based on textural zoning. Powdered samples all larger veins and matrix were analyzed for stable isotope compositions using bulk IRMS for $\delta^{18}O_{PDB}$ and $\delta^{13}C_{PDB}$ (Table 1). Samples KO16, KO17, and KO18 were analyzed using LA-ICP-MS for trace element concentrations (REE, Y and Mn) and SIMS for $\delta^{18}O_{PDB}$ only. Ablation transects were followed across large (7-12 mm-thick) veins in these samples and across smaller fractures (200 μm to 2 mm-thick). Following SIMS analysis, offcuts were imaged in CL. Obtaining reliable fluid inclusion data from these types of rocks is challenging (e.g., Kenis et al., 2000; Bussolotto et al., 2015). Ten double-polished sections were prepared for each sample, and only one from sample KO18 had inclusions suitable for analysis.

4. Results

4.1. All samples

The rock matrix from a majority of the samples have positive $\delta^{13}C_{PDB}$ values from +0.5 to +2.1‰ (Table 1, Fig. 4), within range of marine limestones world-wide (0 ± 5‰, Hudson, 1977; Hoefs, 1997) and those from along the NAF (Janssen et al., 1997, 2009). The

Table 1
Bulk isotope ratio mass spectrometry oxygen ($\delta^{18}O$) and carbon ($\delta^{13}C$) data.

Sample[a]	$\delta^{18}O(‰)_{PDB}$[b]	$[\delta^{18}O(‰)_{PDB}]M-[\delta^{18}O(‰)_{PDB}]V$[c]	$\delta^{18}C(‰)_{PDB}$[b]	$[\delta^{13}C(‰)_{PDB}]M-[\delta^{13}C(‰)_{PDB}]V$[c]
Along the main trace of NAF				
KO14: N 40°41′34.3″; E 36°42′9.1″				
Matrix	−5.4	1.1	2.1	−0.2
Vein	−6.5		2.3	
KO16: N 40°38′23.6″; E 36°50′4.48″				
Matrix	−10.8	−2.1	−8.3	−0.9
Vein	−8.64		−7.30	
Vein duplicate	−8.74		−7.40	
KO17: N 40°37′54.4″; E 36°50′58.4″				
Matrix	−7.8	0.4	0.5	4.6
Vein	−8.1		−4.1	
Vein duplicate	−8.2		−4.1	
KO18: N 40°36′26.8″; E 36°54′56.7″				
Matrix	−7.2	1.6	0.5	0.5
Vein	−8.8		0.0	
Within the Erbaa-Niksar basin				
KO10: N 40°38′22.6″; E 36°44′36.7″				
Matrix	−8.3	2.1	1.5	0
Vein	−10.4		1.5	
KO12: N 40°39 50.1″; E 36°41′10.7″				
Matrix	−8.3	6.3	1.4	0
Vein	−14.6		1.4	

[a] Sample number is KO#. Vein or matrix analysis are indicated. See Fig. 1 for sample locations. In some cases, more than 1 analysis of the vein was obtained as indicated by "duplicate".
[b] Values of $\delta^{13}C$ v. PDB and $\delta^{18}O$ v. PDB done by analyzing standard NBS19 (Coplen, 1994). All errors are ±0.1‰.
[c] Difference in isotopic values of the matrix - vein.

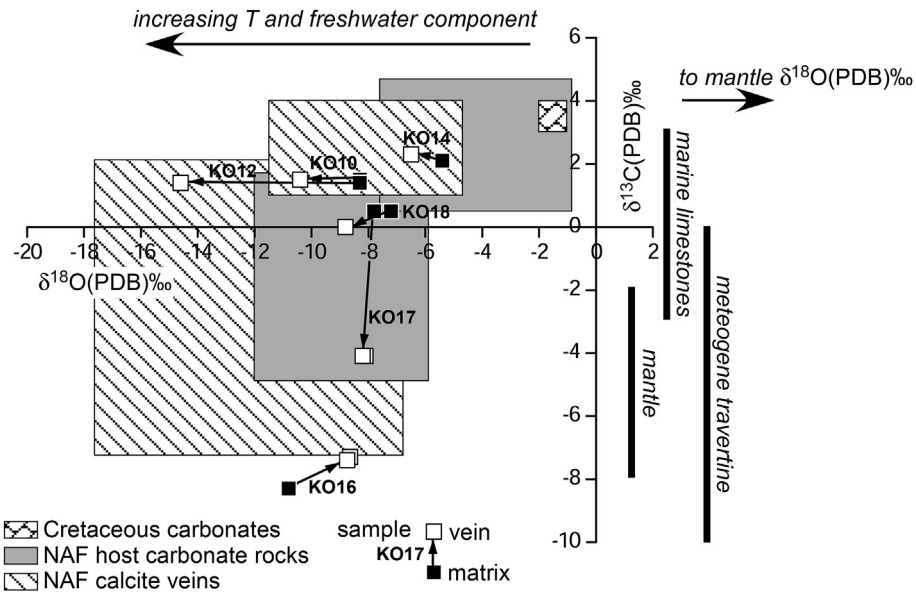

Fig. 4. Cross plot of $\delta^{18}O_{PDB}$ vs. $\delta^{13}C_{PDB}$ for IRMS analyses of calcite matrix and veins. Arrows point from matrix to vein analysis. Regions of previous data from calcite veins and matrix displaced by the NAF are shaded (Janssen et al., 1997, 2009). Area defining average Cretaceous carbonates after Morad et al. (2010).

exception to this is sample KO16, which has a matrix with $\delta^{13}C_{PDB}$ of −8.3‰. This is consistent with origin as a meteogene travertine ($\delta^{13}C_{PDB}$ between −12‰ and 0‰; Pentecost, 2005; D'Alessandro et al., 2007; El Desouky et al., 2015). Vein calcite $\delta^{13}C_{PDB}$ from the majority of the rocks are also within range of marine limestone values, with the exception of samples KO16 (−7.4‰, average of 2 analyses) and KO17 (−4.1‰, average of 2 analyses). All rocks have <1‰ difference between matrix and vein values of $\delta^{13}C_{PDB}$, with the exception of sample KO17, which has a vein that is 4.6‰ lower in $\delta^{13}C_{PDB}$ compared to the rock matrix. This rock and sample KO18 are the only samples to show this trend towards lower $\delta^{13}C_{PDB}$ from matrix to vein.

The $\delta^{18}O_{PDB}$ for the matrix of the samples range from −5.4‰ (sample KO14) to −10.8‰ (sample KO16) (Table 1, Fig. 4), whereas the vein analyses range from −6.5‰ (sample KO14) to −14.6‰ (sample KO12). The matrix values are consistent with marine limestones (−2 to −10‰ $\delta^{18}O_{PDB}$; Hudson, 1977). All samples trend towards lower $\delta^{18}O_{PDB}$ values for vein analyses compared to the matrix, with the exception of sample KO16, which has higher $\delta^{18}O_{PDB}$ in the vein compared to the matrix.

The magnitude difference of $\delta^{18}O_{PDB}$ values between matrix and vein calcite varies. Sample KO17 shows only a 0.4‰ difference, despite its large change $\delta^{13}C_{PDB}$. Sample KO12 preserves $\delta^{18}O_{PDB}$ values that are 6.3‰ lower than the co-existing vein calcite. This and sample KO10 were collected within the Erbaa-Taşova Basin, and have distinct isotopic characteristics from those located exactly on the NAF: lower $\delta^{18}O_{PDB}$ values of the host rock and a larger difference in $\delta^{18}O_{PDB}$ values between the vein and matrix (Table 1), suggesting that the fluid regime in the basin may differ from that along the NAF.

Overall, the focus of this study is the NAF specifically, thus we selected samples KO16, KO17, and KO18 for LA-ICP-MS for trace element data and SIMS for $\delta^{18}O_{PDB}$. These samples were collected from the main trace of the NAF along a portion where normal faulting forms a releasing bend of the Niksar basin (Fig. 2).

4.2. Sample KO18

The matrix limestone in sample KO18 is a pink-grey, fine-grained micrite with stylolites and fractures filled with Fe/Mn-oxide and/or clear calcite (Figs. 3F and 5). The large vein that is the focus for geochemical and fluid inclusion analysis has a sharp boundary with the rock matrix. Multiple, smaller (200 μm to 1 mm-wide) fractures intersect the vein and themselves. These fractures contain brown material (likely Fe/Mn-oxides) or clear calcite. Based on cross-cutting relationships, these fractures contributed material to the main vein. Some smaller veins show an en-échelon pattern, and stylolites intersecting the main vein are present in the matrix. The vein itself has a drusy fabric, with smaller calcite crystals near the matrix contact and large and blocky crystals in its center. This type of growth suggests the vein can be classified as mode-I.

Calcite crystals within the vein are divided into two generations based on textural observations and geochemical differences (Figs. 5 and 6). The first generation is separated into zones A and B based on differences in color, but has flat Mn zoning with similar Mn/REE contents. These zones have similar Mn and lower REE contents as the matrix. A second calcite generation termed zone C is separated from the first based on the presence of darker material that sharply increases in Y and REE, decreases in Mn. After zone C, Mn, Y, and REE contents steadily increase in zone D. Some analyses of zone C material have similar Mn as the matrix, but higher REE. Zone D contains clear, euhedral crystals with the lowest Mn and REE (Figs. 5 and 6). Overall, the vein is enriched in LREE compared to HREE across all zones.

REE patterns within the vein zones are similar in shape with different magnitudes, with all being relatively flat with negative Ce and positive Y anomalies when normalized to chondrite or shale (Fig. 7A and B). We explored numerous shale and chondrite normalization schemes (SN and CN; e.g., Haskin and Haskin, 1966; Sun and McDonough, 1989; Piper, 2001), and all show consistent patterns. The zones and the matrix have negative Eu anomalies, except for zone D. The matrix and zone C share similar HREE contents, but zone C is more enriched in LREE, suggesting an addition of these components via sources other than those derived from the matrix (Fig. 6D). Zone C appears unique compared to the other regions in that a majority of its analyses have $La_{SN}/Yb_{SN} > 1$ and $Gd_{SN}/Yb_{SN} < 1$. All zones have Y_{CN}/Ho_{CN} slightly >1. Zone D has the lowest REE contents and REE_{CN} and REE_{SN} values.

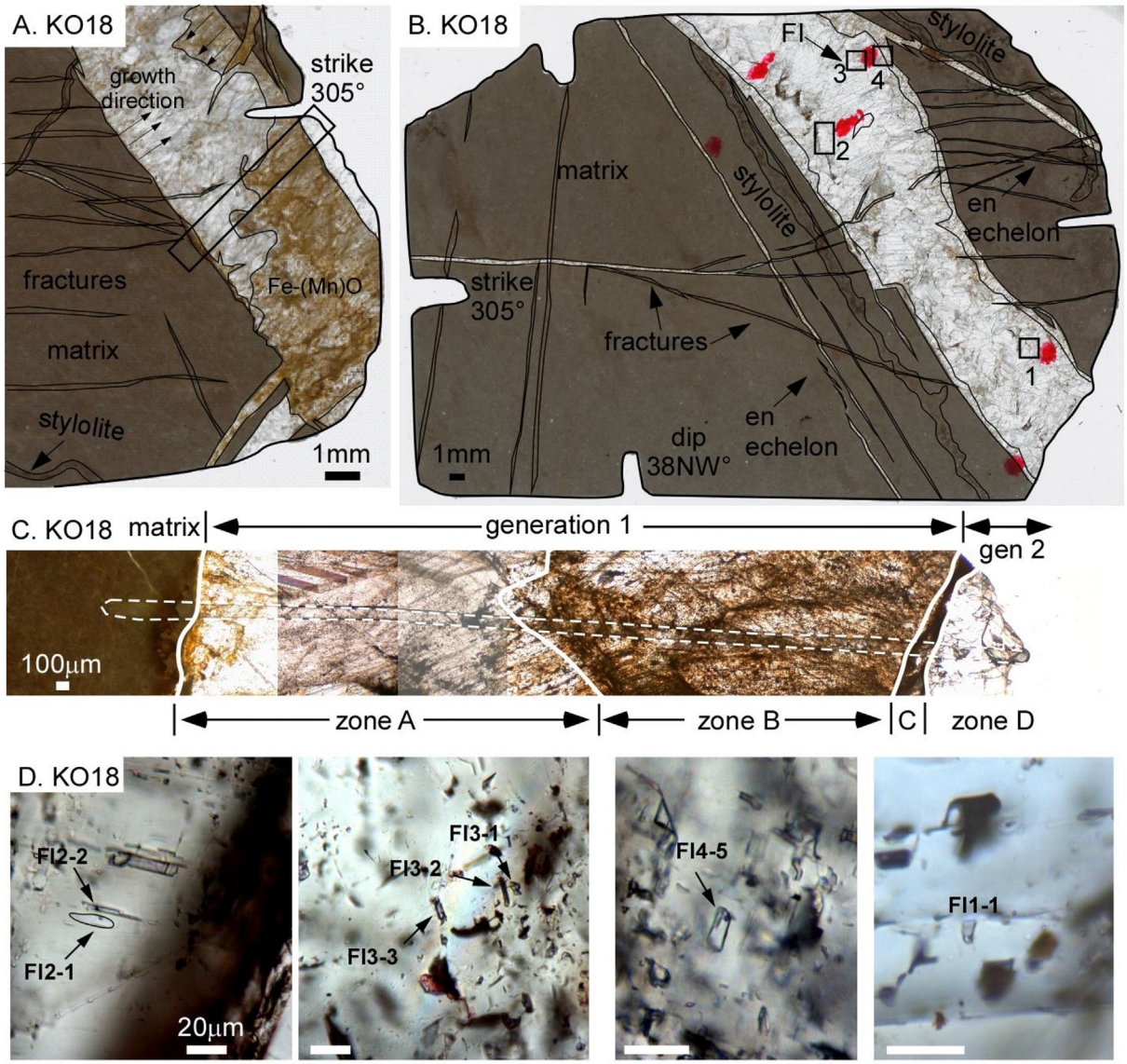

Fig. 5. (A and B) Thin section scans of sample KO18. Matrix, fractures, and vein are labeled. Panel B indicates the regions where fluid inclusion analyses were identified and analyzed as boxes. Inset in panel (A) shows the location of (C), a petrographic image of the laser scan across the matrix and vein region in the sample. The vein is subdivided into two generations, which are further subdivided into zones. (D) Images of selected fluid inclusions. See Table 2 for conditions and Supplementary data for images of all inclusions. Red dots are ink stains used to locate fluid inclusions.

An offcut of the region analyzed using LA-ICP-MS was used for fluid inclusion temperature estimates (Fig. 5B, Table 2). This offcut only contains generation 1, and inclusions are grouped into four regions. Temperatures obtained for fluid inclusions (T_h, °C) range of 83.8 °C to 96.1 °C with an average of mean of 83.8 ± 7.3 °C (±1σ, Table 2). These values are within what has been reported for calcite veins collected elsewhere along the NAF (70 °C–170 °C; Janssen et al., 1997, 2009). Neighboring inclusions <5 μm apart yield T_h that differ by ~20° (Fig. 5D). The highest T_h measured (96.1 °C) is located ~1.5 mm from the vein wall, whereas the lowest T_h (72.3 °C) is ~2 mm from the vein wall opposite the inclusion with the highest calculated T_h. Ice melting temperatures (T_m) for the inclusions were challenging to obtain due to their small size.

Four $\delta^{18}O_{PDB}$ SIMS transects were made across an offcut of the vein in sample KO18: two were made perpendicular to opposite sides of the matrix (transects 1 and 2), one parallels the southern matrix contact (transect 3), and another termed the fracture transect, located at an intersection between the vein and a fracture that extends from the main body (Fig. 8). The majority of the vein is dark, but regions of brighter CL are found along cracks separating individual large grains, as isolated zones of brecciated alteration, along grain boundaries, and as patchy zones overprinting darker grains. The $\delta^{18}O_{PDB}$ value for the same vein measured using SIMS average −8.8 ± 0.3‰ (n = 35 spots) with Mean Square Weighted Deviation (MSWD) of 28. Despite the similarity to the IRMS value of the vein of −8.84‰, the $\delta^{18}O_{PDB}$ values obtained using SIMS vary along transects perpendicular to the matrix. The total variation along transect 1 is 6.5‰ and along transect 2 is 3.3‰. Transect 3 parallel to the matrix wall averages $\delta^{18}O_{PDB}$ of −9.7 ± 0.3‰ (n = 7 spots, MSWD = 1), and a smaller fracture intersecting the vein averages −7.8 ± 0.3‰ (MSWD = 1.5). The smaller fracture results are similar to the IRMS $\delta^{18}O_{PDB}$ obtained from the rock matrix (−7.2‰). Transect 2 and the fracture are located near each other, and yield $\delta^{18}O_{PDB}$ SIMS values that overlap (from −8.2 ± 0.2‰

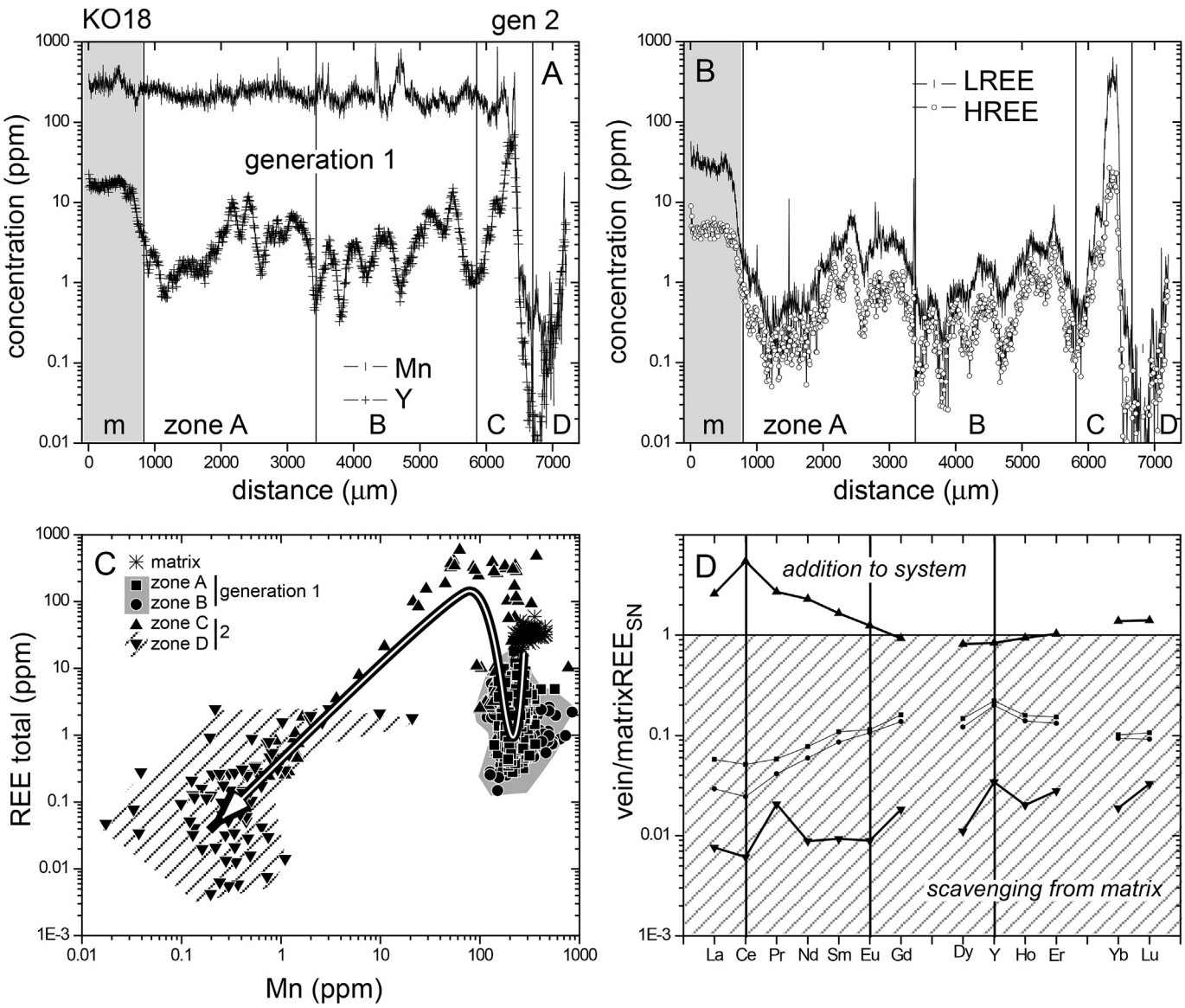

Fig. 6. LA-ICP-MS compositional transects across the vein in sample KO18 (Fig. 5A, C) in (A) Mn and Y, (B) LREE and HREE. REE are La, Ce, Pr, Nd, Sm, Eu, Gd (LREE), Dy. Ho, Er, Yb, and Lu (HREE). (C) Plot of Mn vs. REE total with regions of generations 1 and 2 distinguished by shading. (D) REE patterns of vein/matrix REE_{SN}. Area where vein/matrix REE_{SN} is ≤ 1 is suggested to be the result of interaction with the matrix termed "scavenging." Region where REE_{SN} >1 suggests addition to the vein by sources external to the matrix.

to −7.3 ± 0.3‰ along the fracture compared to from −9.8 ± 0.3‰ to −6.8 ± 0.2‰ for transect 2) (Fig. 8B and C).

4.3. Sample KO16

Sample KO16 was collected less than 1 km north of the active trace of the NAF (Fig. 2) in a region mapped as an anticline (Aktimur et al., 1990; Herece and Akay, 2003). The sample is a travertine and contains microcrystalline calcite growth bands within its matrix (Fig. 9). The sample is partially brecciated, with microcracks and fractures between and across growth bands. A single large vein within the sample was analyzed using SIMS and LA-ICPMS, and contains solid inclusions of calcite forming along growth zones. We divided three mineral generations within the vein based initially on petrographic textures that are distinct geochemically. Within the first two generations (1 and 2), we label five zones (A-E) that show different Mn, Y and REE contents (Fig. 10).

The first generation (zones A and B) is located adjacent to the matrix and exhibits larger amounts of sediment compared to the remainder of the vein. Oscillations in the amount of sediment incorporated into the crystals is seen as nesting angular forms facing point outward into the center of the vein and is consistent with crack-seal growth (Fig. 9) (Ramsay, 1980). Crystal size in this generation ranges ~0.5–1 mm in width perpendicular to growth direction and 1–2 mm in length parallel to growth direction. The boundary between zone B and C marks the end of the first mineral generation and is also identified by a sharp decrease in Mn and the beginning of a gradual decrease in Y and REE (Fig. 10).

The second mineral generation is divided into zones C, D and E that contains clearer calcite crystals (Fig. 9). Although this generation has the largest crystals in the vein (~4 mm in length and ~2 mm in width), smaller crystals appear confined to boundaries. The dominant growth direction is from generation 1 to generation 3. No preferential c-axis alignment is seen in crossed polarized light. Finer-grained crystals are located at the end of the second mineral generation.

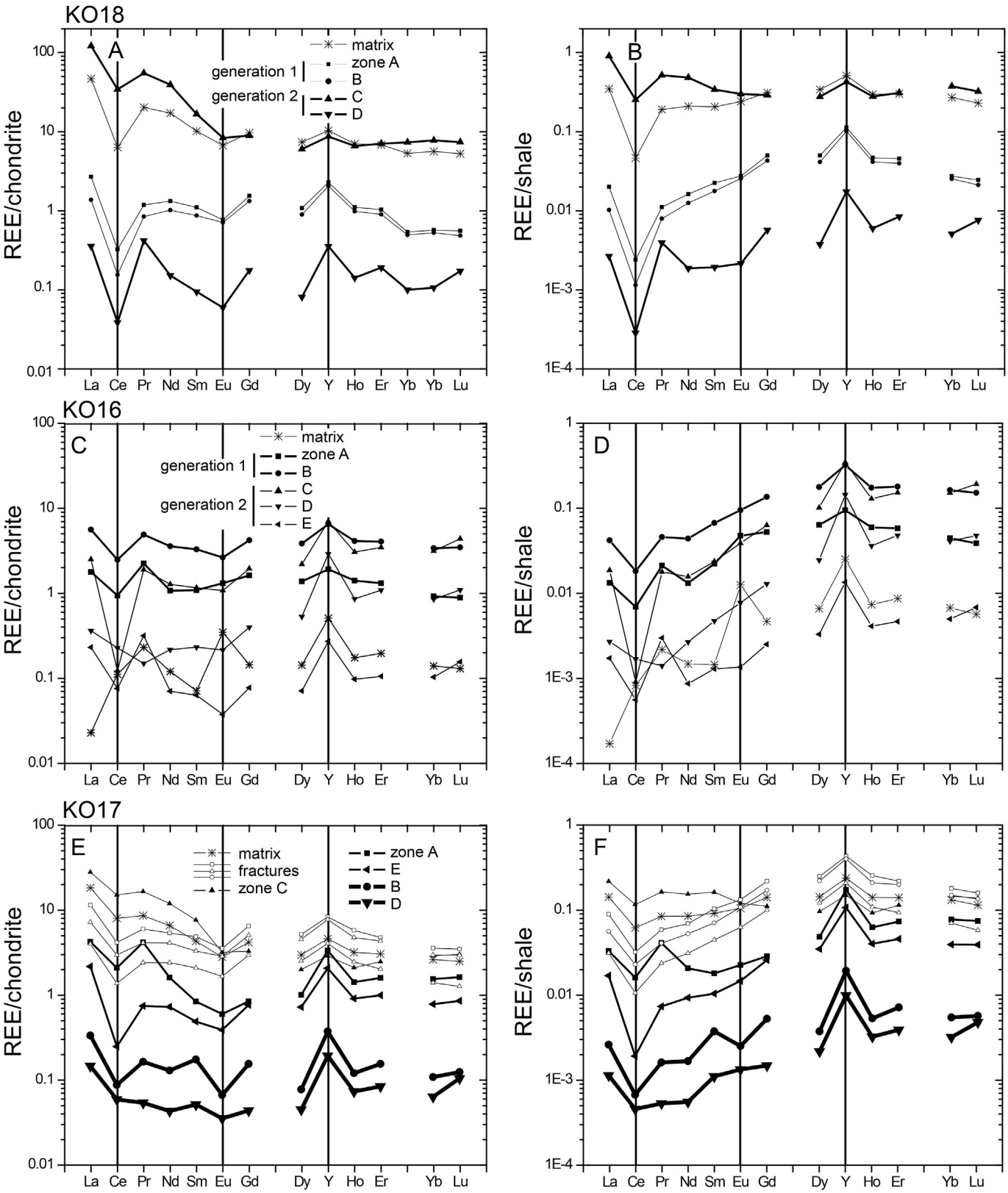

Fig. 7. REE patterns normalized to (A, C, E) chondrite (Sun and McDonough, 1989) and (B, D, F) shale (Haskin and Haskin, 1966; Piper, 2001). Analyses across the vein in sample KO18 is shown in panels (A and B). Panels (C and D) show analyses across the vein in sample KO16, and panels (E and F) show analyses across the vein in sample KO17.

Table 2
Fluid inclusion data for sample KO18.

Analysis[a]	T_h (°C)[b]	T_{hyd}(°C)[c]	T_{lith}(°C)[d]	P_{hyd}(bar)[e]	P_{lith}(bar)[f]
3–1	96.1	105.2	120.4	170.4	453.9
3–2	90.7	99.1	113.2	158.3	421.2
2–2	90.5	98.9	112.9	157.8	420.1
4–3	90.3	98.7	112.7	157.4	418.8
3–5	89.5	97.8	111.6	155.6	414.1
1–1	88.8	97.0	110.7	153.0	409.8
2–3	83.8	91.4	104.0	142.8	379.8
4–1	83.5	91.0	103.6	142.1	378.0
3–4	80.3	87.5	99.4	134.9	358.0
4–2	79.6	86.7	98.5	133.3	354.6
4–5	78.5	85.4	97.0	130.9	348.0
3–3	76.1	82.8	93.8	125.5	333.7
4–4	73.8	80.2	90.8	120.4	320.0
2–1	72.3	78.5	88.8	117.0	311.0
Average (±1σ)	83.8 (7.3)	91.4 (8.2)	104.1 (9.7)	142.8 (16.3)	380.1 (43.8)

[a] Nomenclature: fluid inclusion assemblage and inclusion number. See Fig. 5 and Supplementary data for images.
[b] Homogenization temperature (±0.1 °C), measured by thermal cycling (Goldstein and Reynolds, 1994).
[c] Pressure-corrected temperature assuming $T_m = 0$ °C, salinity = 0%, and a hydrostatic thermobarometric gradient of 50°C/100bar (Goldstein and Reynolds, 1994; Steele-MacInnis et al., 2012).
[d] Pressure-corrected temperature assuming $T_m = 0$ °C, salinity = 0%, and a lithostatic thermobarometric gradient of 50°C/226bar (Goldstein and Reynolds, 1994; Steele-MacInnis et al., 2012).
[e] Pressure of formation assuming $T_m = 0$ °C, salinity = 0%, and a hydrostatic thermobarometric gradient of 50°C/100bar (Goldstein and Reynolds, 1994; Steele-MacInnis et al., 2012).
[f] Pressure of formation assuming $T_m = 0$ °C, salinity = 0%, and a lithostatic thermobarometric gradient of 50°C/226bar (Goldstein and Reynolds, 1994; Steele-MacInnis et al., 2012).

The third texturally distinct area (generation 3, Fig. 9) was not analyzed using LA-ICP-MS. This region contains smaller calcite crystals (few μm) interrupted by small areas of larger crystals that grew inward from the surrounding matrix. The area is uneven in width from the left vein wall, which is unlike sediment rich generation 1 on the opposite vein wall. Growth zones and direction are not apparent for the fine calcite within this generation.

All zones within the vein show flat REE patterns when normalized to chondrite and are HREE-enriched compared to LREE when normalized to shale (Fig. 7C and D). Regardless of normalization scheme, the matrix yields a unique pattern with La depletion and a positive Eu anomaly that differs from the vein zones. All areas analyzed show positive Y anomalies and most have negative Ce anomalies, with the exception of the matrix and zone D. Zones of generation 1 have largely similar REE patterns, although zone A does not have a negative Eu anomaly. Most zones have higher amounts of REE_{SN} in general than the matrix, with the exception of zones D and E. The majority of LA-ICP-MS analyses of the vein have $Y_{CN}/Ho_{CN} > 1$, with analyses following a loop of increasing values from generation 1 to 2. As the transect moves from the matrix to zone E, La_{SN}/Y_{SN} and Gd_{SN}/Yb_{SN} follow a counter-clockwise loop that increases then decreases in these values.

Nineteen SIMS spots were placed across a polished offcut of the vein analyzed by LA-ICP-MS within generations 1 and 2 (Fig. 11). The CL image of the sample shows that the matrix and generation 1 have brighter luminescence than the other portions of the vein, likely related to Mn contents. The average SIMS $\delta^{18}O_{PDB}$ of the vein is −9.7 ± 0.3‰ (±2σ, MSWD = 45), which lies in between the IRMS $\delta^{18}O_{PDB}$ values of the vein (−8.69‰) and matrix (−10.9‰; Table 1). The total variation of SIMS $\delta^{18}O_{PDB}$ ranges from −16.7 ± 0.6‰ to −7.4 ± 0.3‰, depending on location. The low value is problematic as analyses adjacent to this spot differ significantly. Discounting this analysis, $\delta^{18}O_{PDB}$ increases from vein wall in generation 1 towards the vein center in generation 2. The increase is gradual in $\delta^{18}O_{PDB}$ from −13.6 ± 0.3‰ towards −10.2 ± 0.2‰ in zone A and plateaus at −8.8 ± 0.4‰ in zone B and −8.5 ± 0.3‰ in generation 2, similar to the $\delta^{18}O_{PDB}$ results from the vein obtained using IRMS.

4.4. Sample KO17

Sample KO17 was taken directly from the principal strand of the NAF (Figs. 2 and 3E). The limestone is a brown to yellowish fine grained micrite, massively bedded with no evident allochems. Small fractures (10–100 μm) filled with calcite crystals are abundant. These fractures cross-cut each other and a large vein in the center of the sample (Fig. 12). The large calcite vein in the center of sample KO17 shows differences in crystal size and sediment incorporation. Calcite crystals grew inward from the matrix on each side of the vein, increasing in size substantially from 10 μm to >1 mm as distance increases.

The calcite vein in sample KO17 is divided into three textural associations labeled as generations (Figs. 12 and 13). The first contains calcite crystals adjacent to a vein wall with distinct zoning and a high density of very fine sediment trapped in the crystal structure. This generation is also labeled as zone A and is not present at some locations within the larger vein. Crystals in this group are elongated compared to others, with lengths commonly >1 mm, and widths of ~0.5 mm. The second generation in the center of the vein has larger crystals (>1 mm wide to 2 mm long) that are clearer and less elongated than those seen in the first generation. This generation is subdivided into three zones (B, C, and D). Larger, clear calcite crystals in zone B have euhedral boundaries and are coated by fine grained carbonate cement (zone C). Voids border zone C and comprise the center of this vein. A similar zone of large, clear euhedral calcite (zone D) also coated in carbonate cement is located on the other side of the central void. Generation 3 (zone E) is

Table 3
Earthquakes (1900–2017) information in the field area (Fig. 1).[a]

Time (UTC)	Latitude	Longitude	Depth (km)	Type	Magnitude
10/9/2015 16:11	40.668	36.674	20.52	Mw	4.0
10/9/2015 14:39	40.664	36.681	20.17	Mw	4.9
3/7/2013 21:50	40.815	36.169	20.62	Ml	4.3
8/29/2005 22:33	40.621	36.884	10	mb	4.0
7/7/2005 19:33	40.490	37.360	2	mb	4.1
2/3/2004 11:50	40.650	36.520	1	mb	4.1
9/27/2003 19:34	40.604	35.877	3.1	mb	4.0
5/3/2001 6:10	40.634	36.661	6.4	mb	4.1
12/1/1996 16:33	40.476	37.223	25.2	mb	4.3
7/29/1996 22:04	40.850	36.240	5	mb	4.1
6/12/1993 8:58	40.576	35.880	10	mb	4.4
6/3/1993 7:46	40.919	35.980	10	mb	4.2
5/12/1992 23:38	40.834	35.908	18.1	mb	4.4
2/12/1992 15:59	40.559	35.949	5.6	mb	4.9
4/6/1984 22:13	40.520	36.632	12.9	mb	4.1
12/7/1981 21:17	40.657	36.003	10	mb	4.5
7/15/1975 21:59	40.878	36.058	27.7	mb	4.7
7/10/1970 13:30	40.909	35.983	39.2	mb	4.5
4/1/1962 1:39	40.800	36.100	10	MS	4.7
7/26/1960 12:36	40.560	37.250	40	MS	4.6
12/20/1942 14:03	40.870	36.470	10	MS	7.0
12/28/1939 3:25	40.470	37.000	40	MS	5.7
12/27/1939 22:34	40.830	36.800	10	MS	4.9
12/27/1939 20:00	40.800	36.800	30	MS	4.5
6/21/1908 3:55	40.600	35.900	10	MS	5.2
3/28/1907 0:00	40.490	37.170	10	MS	4.8
5/15/1905 0:00	40.500	37.000	10	MS	4.8
2/3/1902 22:00	40.630	36.790	10	MS	4.4

[a] Data from the Republic of Turkey Prime Ministry Disaster and Emergency Management Authority database (http://deprem.gov.tr/). See Fig. 1 for epicenters of these earthquakes.

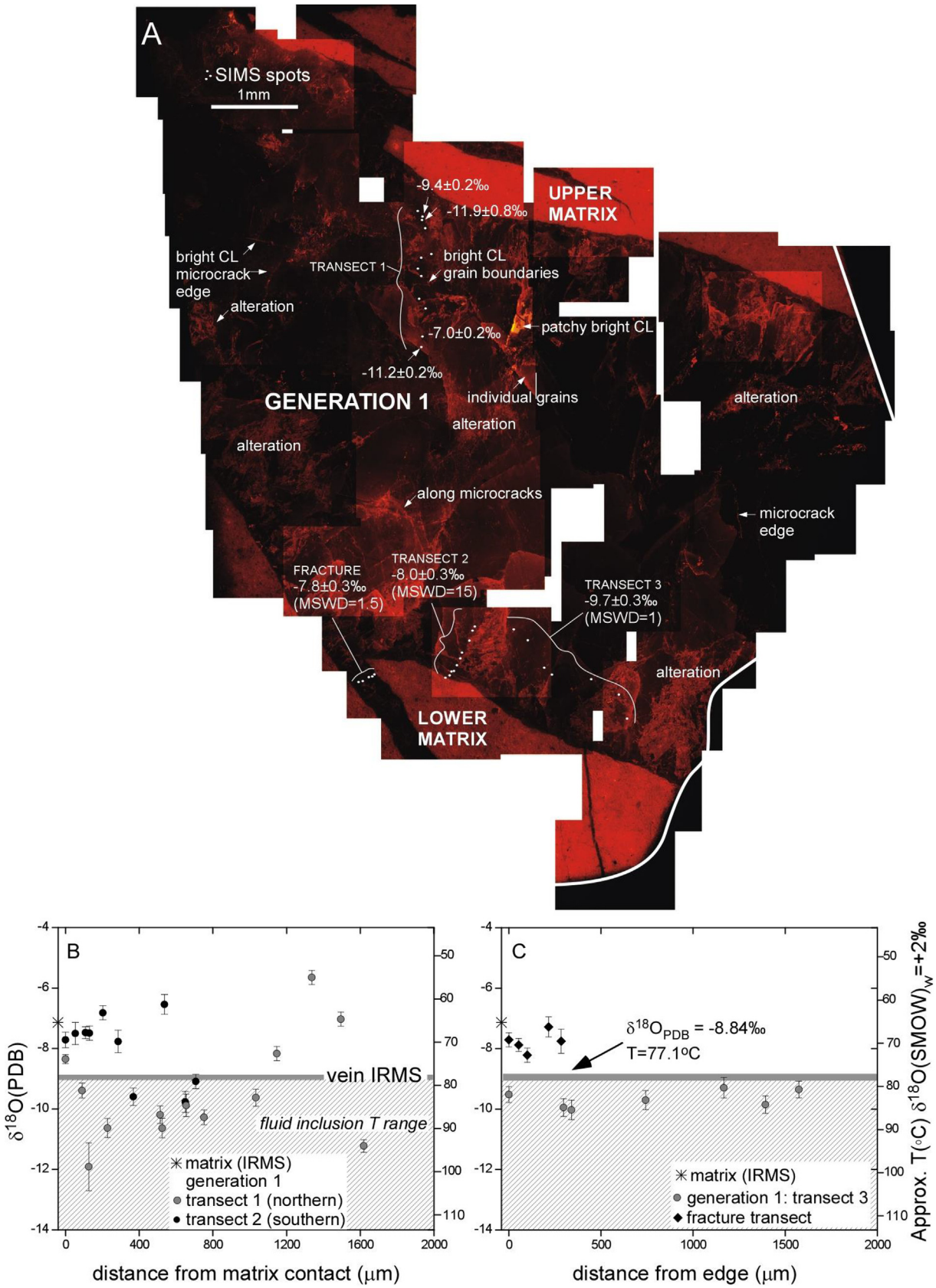

Fig. 8. (A) Composite of CL images of sample KO18. The region is an offcut of the thin section in Fig. 5A. Regions where SIMS $\delta^{18}O_{PDB}$ analyses were obtained and some $\delta^{18}O_{PDB}$ ($\pm 2\sigma$) are identified. See Supplementary data for analytical information. Areas of brighter CL are indicated. These are typically along microcracks and in textures indicative of post-crystallization alteration (patchy textures and along grain boundaries). SIMS $\delta^{18}O_{PDB}$ values across (B) generation 1, transects 1 and 2, and (C) generation 1, transect 3 and across the fracture in sample KO18. These values have been translated to temperature (°C) assuming isotopic equilibrium with Cretaceous brines ($\delta^{18}O_{SMOW\text{-}fluid} = +2‰$) (Morad et al., 2010) using calibration of Hays and Grossman (1991). IRMS $\delta^{18}O_{PDB}$ value is indicted of the vein (horizontal line) and matrix (star). Region of fluid inclusion temperatures is shaded.

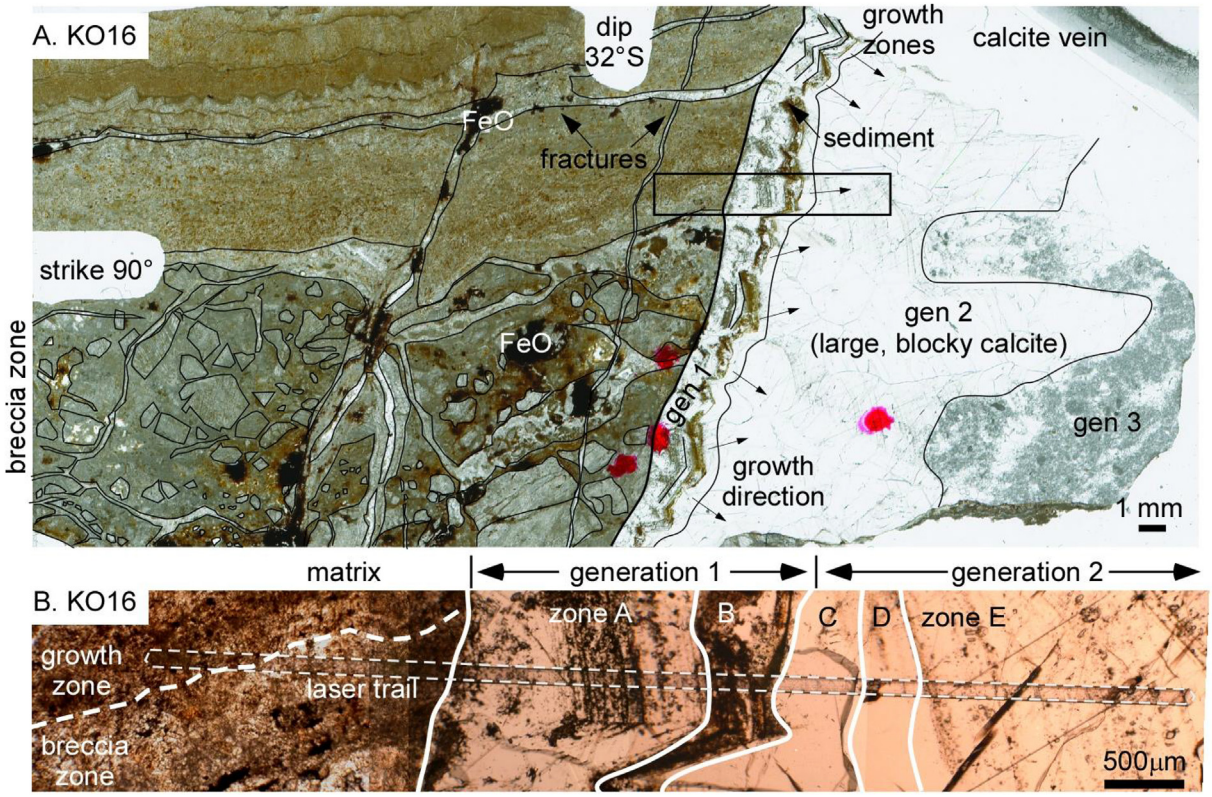

Fig. 9. (A) Thin section scan of sample KO16. Calcite generations (gen), fractures, iron oxides, and regions in the matrix and vein are labeled. Inset shows the location of (B), a petrographic image of the laser scan across the matrix and vein region in the sample. The vein is subdivided into three generations, which are further subdivided into zones.

located adjacent to the large calcite crystals, on the opposite vein wall from generation 1. This region contains the smallest calcite crystals within the vein (~10 μm wide) in alternating dark bands <1 mm in width. Each band is bounded by a dark area of fine carbonate material. Like generation 1, it is not always present within the vein.

The textural zones are also chemically distinct, with higher Mn + Y + REE contents seen in zone C and the matrix (Fig. 13A and B). We found that LA-ICP-MS analyses of the matrix and small fractures contain similar or higher Mn and REE contents compared to the vein. The zones located nearest the matrix (A and E) overlap in composition and have lower amounts of Mn than the matrix. Zones B and D, located on either side of the center zone C, also have similar REE and Mn contents (Fig. 13C and D). Zone C partially overlaps with matrix in Mn and REE contents. Oscillations in the amount of Mn relates to the presence of darker material within the calcite veins. Zones A and C and part of zones B and E have more LREE, whereas the other regions show roughly similar LREE and HREE contents (Fig. 13B).

The REE patterns in samples KO17 differ depending on zone analyzed. Most are LREE enriched compared to chondrite, or are flat or HREE-enriched if normalized to shale (Fig. 7E and F). Regardless of normalization scheme, all zones have REE patterns with negative Ce anomalies and positive Y anomalies. Only zone B has a negative Eu anomaly. The matrix, smaller fractures, and zone C are largely similar, as are patterns for zones B and D and zones A and E. When compared to the matrix, the majority of the veins have vein/REE_{SN} values of <1, with the exception of minor increases in $LREE_{SN}$ in zone C and $HREE_{SN}$ in the fracture analyses. Most analyses have $Y_{CN}/Ho_{CN} > 1$, but define different trends depending on zone analyzed. Zone D is unique in that it displays superchondritic values of Y_{CN}/Ho_{CN} (>40). Most zones have $La_{SN}/Yb_{SN} > 1$, with the exception of central zone C and some matrix analyses. Most zones have $Gd_{SN}/Yb_{SN} < 1$, with the exception of some analyses of the smaller fractures, zone C, and the matrix.

As with the other samples, the matrix has brighter CL than the majority of the vein calcite (Fig. 14) due to higher Mn and REE concentrations. CL shows that pieces of the matrix with long axis parallel to the vein wall are included within the vein in generation 3. Vein calcite exhibits a nearly uniform lack of luminesce throughout all mineral generations, with the exception of small regions in zone C on either side of the central void. The shape of the bands suggests that they follow a growth zone or euhedral boundary in the vein calcite, and is continuous through all imaged areas on either side of the central void. This is due to the presence of sediments that coat the crystals bordering the void. The brightest areas in the center of the vein are small calcite grains that lie within the carbonate sediment, closest to the center of the vein.

Multiple SIMS spots were placed on the large central vein and five parallel fractures (Figs. 14 and 15). Overall, two SIMS transects are located across the vein's generation 2 and three transects were made across generation 3. The sample did not contain generation 1, which varies in thickness. In addition to the vein analyses, spot analyses were obtained from several smaller fractures that parallel the larger central vein. The average $\delta^{18}O_{PDB}$ of all SIMS results across the larger calcite vein (58 spots) in sample KO17 is −8.7 ± 0.6‰ with a MSWD of 5, similar to the average IRMS vein value is of −8.11‰. However, the $\delta^{18}O_{PDB}$ variation ranges from −6.8 ± 0.7‰ (zone C in generation 2) to −11.0 ± 0.4‰ (zone D in generation 2). The matrix $\delta^{18}O_{PDB}$ obtained using IRMS is −7.8‰. SIMS values for $\delta^{18}O_{PDB}$ increase with distance from matrix along transect 2 across generation 2 (n = 3 spots), and along transect 1 across generation 3 (n = 7 spots). Smaller fractures show a larger total $\delta^{18}O_{PDB}$ variation from −15.9 ± 0.4‰ to −4.8 ± 0.5‰. We

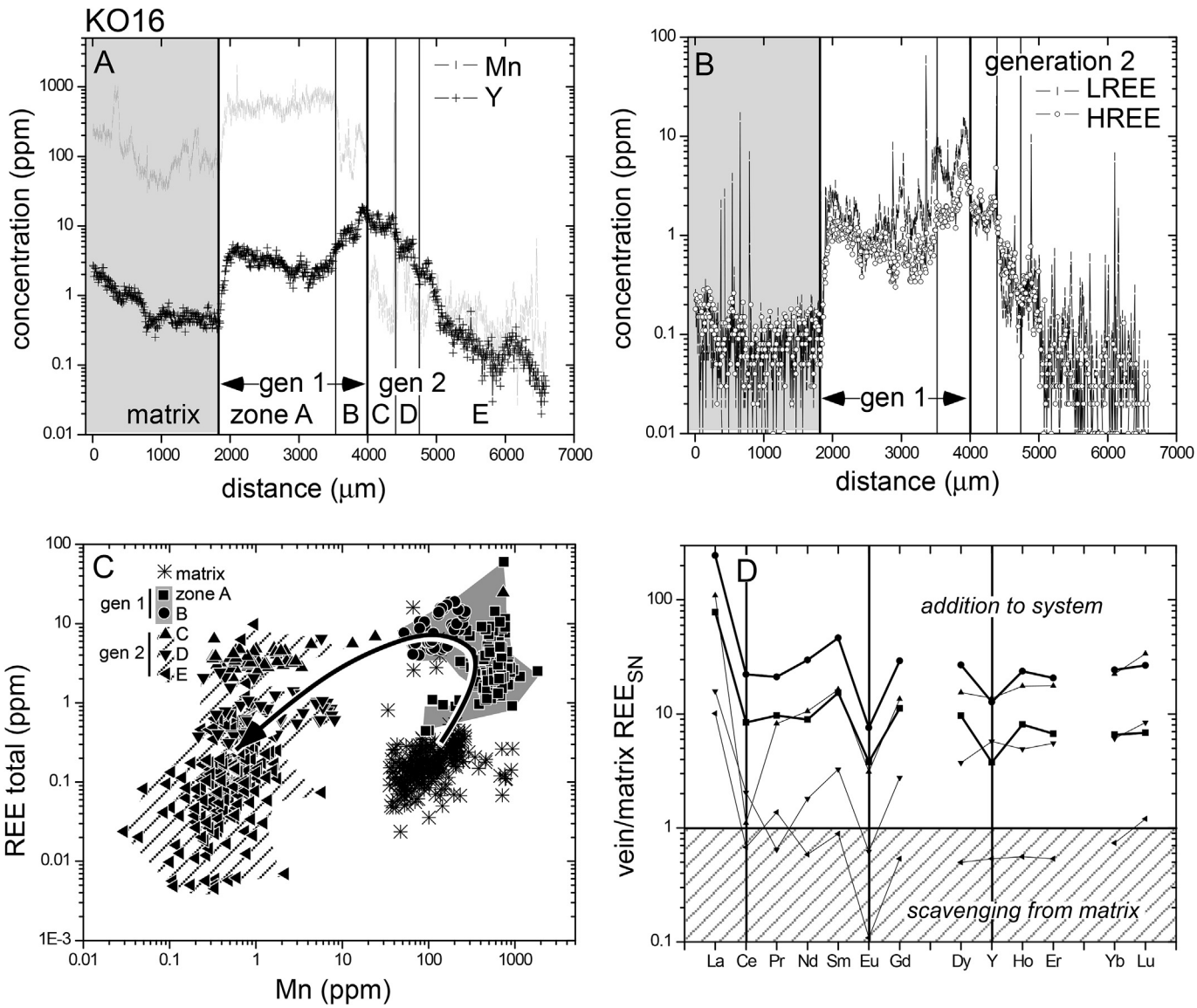

Fig. 10. LA-ICP-MS compositional transects across the vein in sample KO16 (Fig. 9) in (A) Mn and Y, and (B) LREE and HREE. REE are La, Ce, Pr, Nd, Sm, Eu, Gd (LREE), Dy. Ho, Er, Yb, and Lu (HREE). (C) Plot of Mn (ppm) vs. REE total (ppm) for KO16 analyses. Regions of generation 1 and 2 are shaded. The arrow connects the average values of the matrix and vein zones and follows the LA-ICP-MS transect from matrix to generation 2. (D) REE patterns of vein/matrix REE_{SN}. Area where vein/matrix REE_{SN} is ≤ 1 is suggested to be the result of interaction with the matrix. Region where REE_{SN} >1 suggests addition to the vein by sources external to the matrix.

observe a 6‰ increase in $\delta^{18}O_{PDB}$ along one fracture transect in the top portion of the sample (Fig. 15C). Thinner and thicker vein cross each other in the lower portion of the sample; the thicker fractures show up to 4‰ lower $\delta^{18}O_{PDB}$ values than the thinner fracture. Their intersection point yields a value in range of results from the thicker vein.

5. Discussion

5.1. Mode of vein formation

Deciphering the origin of the calcite veins is facilitated by geochemical and isotopic data. Although six fractured limestone assemblages were collected, we focused on three particular rocks that have characteristics that may be representative of the range of textures and tectonic histories of the limestone assemblages in the field area. Sample KO16, KO17, and KO18 were collected directly from exposures of the NAF (Figs. 1 and 2) and all show crystallization in open fracture space (mode-I) with crack-seal growth as material from the matrix is incorporated at vein edges (Ramsay, 1980) (Figs. 5, 9 and 12). All rocks have smaller fractures adjacent to the larger calcite veins. The presence of stylolites in sample KO18 suggest local dissolution and diffusional transport of material from the matrix to veins. Petrographic and CL textures in samples KO16 and KO18 also imply that the vein calcite, once formed, was not further significantly deformed or altered, and thus are indicators of the conditions and compositions of fluids facilitating mineralization (Figs. 8 and 12). Sample KO17 shows evidence in CL for post-crystallization alteration as brighter patches and regions of breccia are present (Fig. 14). The majority of the sample is dark in CL with alteration localized to areas near the matrix. A relative chronology for all larger veins analyzed in this study is inferred, with older calcite at the vein edge and younger calcite in the center. The distance axis along transects perpendicular to vein walls in SIMS

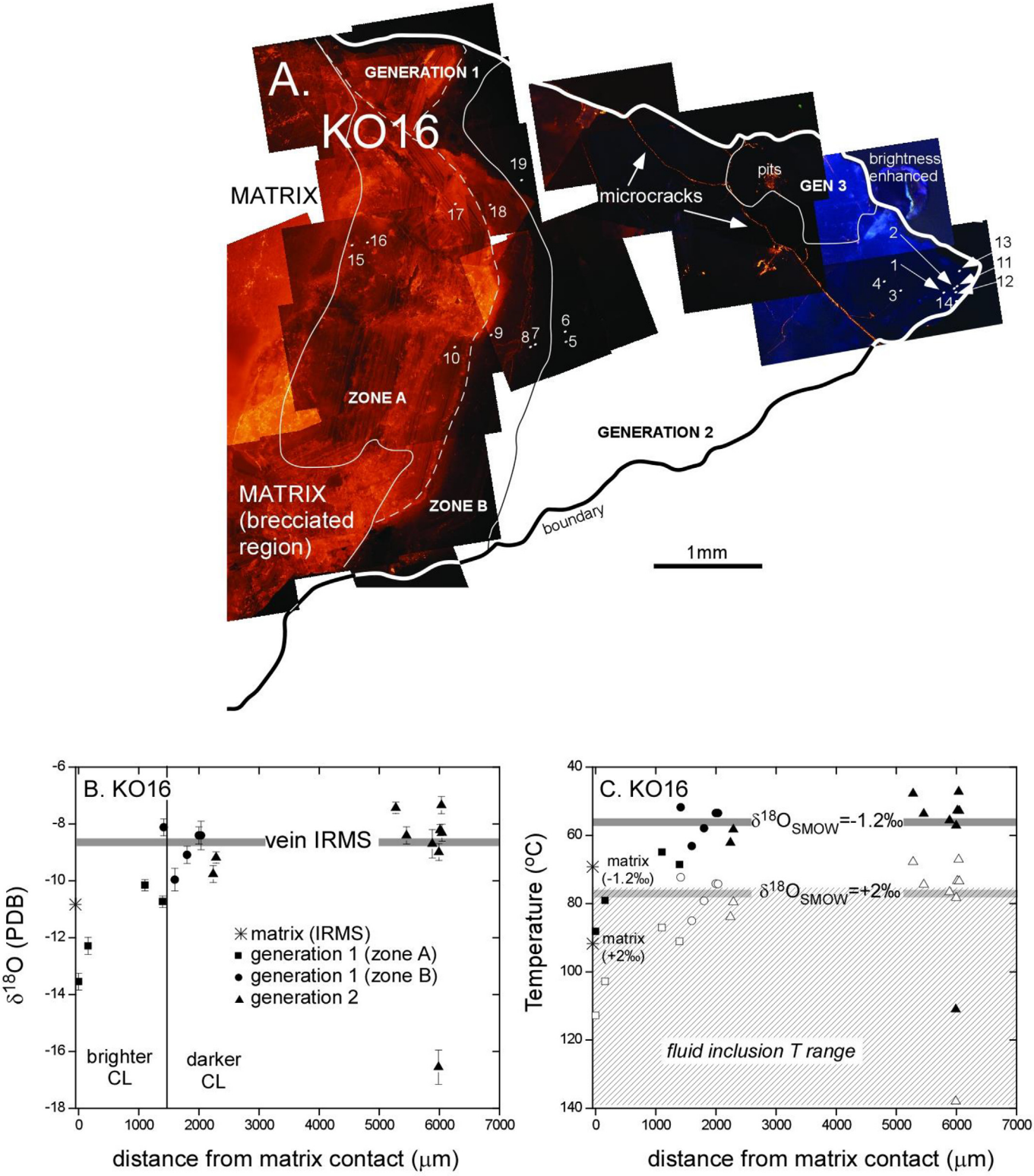

Fig. 11. (A) CL image of sample KO16. The region is an offcut of the thin section in Fig. 9. The matrix calcite and generations (gen) 1 (zones A and B only), 2, and 3 are labeled. Regions where SIMS $\delta^{18}O_{PDB}$ analyses were taken are identified by spot number. The right end of the image has been contrast enhanced as this portion of the vein shows little brightness. See Supplementary data for analytical information. (B) SIMS $\delta^{18}O_{PDB}$ analyses across the vein in sample KO16. (C) Distance vs. temperature (°C) across the KO16 vein assuming isotopic equilibrium with Cretaceous brines ($\delta^{18}O_{SMOW\text{-}fluid} = +2‰$) and seawater ($\delta^{18}O_{SMOW\text{-}fluid} = -1.2‰$) (after Zeebe, 2001; Morad et al., 2010) using calibration of Hays and Grossman (1991). IRMS $\delta^{18}O_{PDB}$ value is indicted of the vein (horizontal line) and matrix (star).

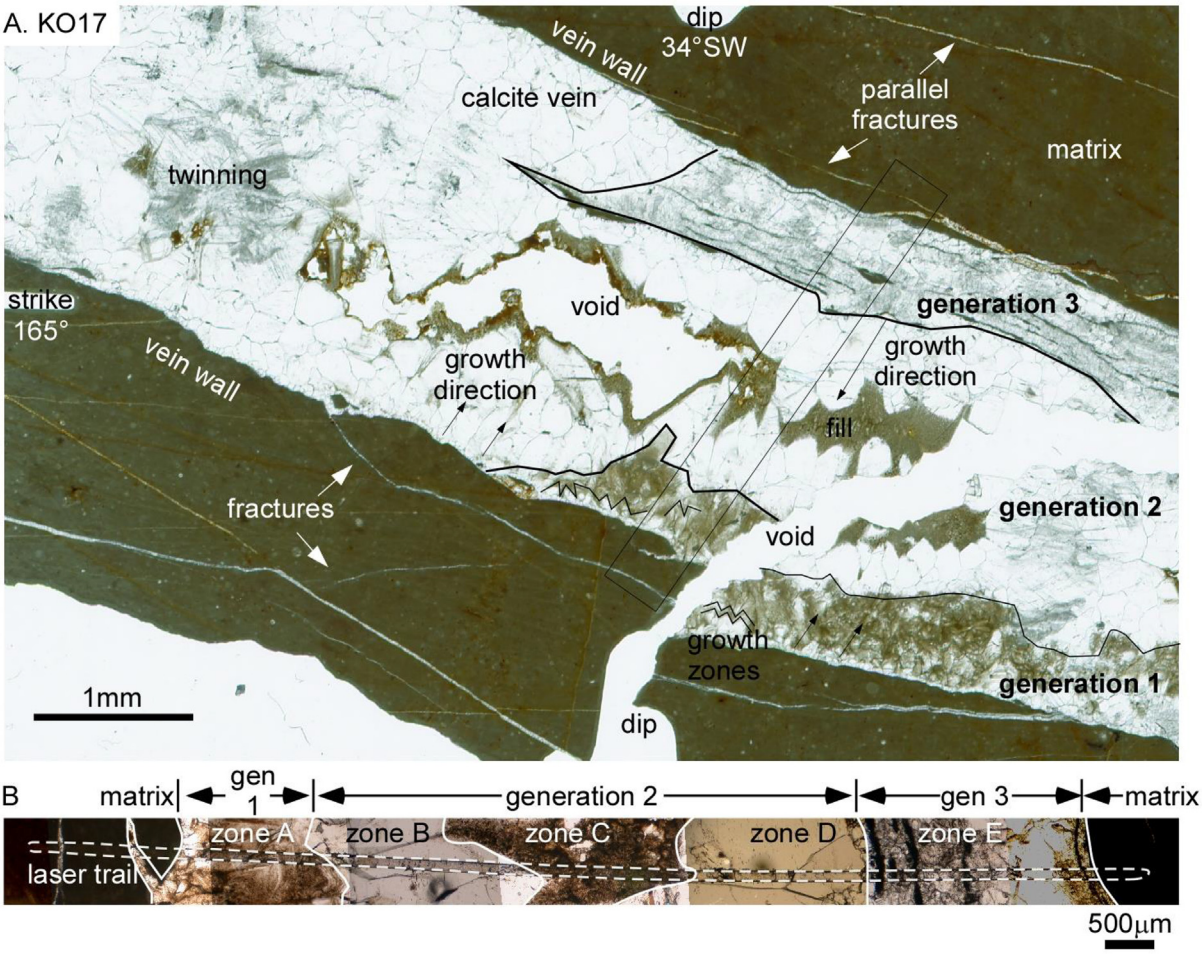

Fig. 12. (A) Thin section scan of sample KO17. Calcite generations (gen), fractures, and regions in the matrix and vein are labeled. Inset shows the location of (B), a petrographic image of the laser scan across the matrix and vein region in the sample. The vein is subdivided into three generations, which are further subdivided into zones.

$\delta^{18}O_{PDB}$ and LA-ICP-MS REE, Mn, and Y can be thus roughly interpreted as time.

5.2. Conditions of vein formation

5.2.1. P-T conditions of vein formation

The average T_h of all inclusions in sample KO18 is 83.8 ± 7.3 °C (±1σ, average of mean). Primary inclusion T_h serves as a minimum entrapment condition for fluid inclusions, which is usually higher due to a pressure correction (Goldstein and Reynolds, 1994). To address this, temperatures were corrected using the isochore approach combining T_h and low salinity estimates (Table 2) (Steele-MacInnis et al., 2012). Temperatures increase by 6–9 °C assuming hydrostatic conditions (50°C/100bar) and by 17–24 °C assuming lithostatic conditions (50°C/226bar). Formation pressures were also estimated through implementation of these thermobarometric gradients, and range from 117bar to 454bar (Table 1). Although uncertainty in the assumptions required to calculate these values exist, vapor bubbles are small (~1–5% of the inclusion volume, Fig. 5), thus it is unlikely that these inclusions formed at high pressure.

Neighboring inclusions <5 μm apart yield T_h that differ by ~20° and ~44bar (Table 2, Fig. 5). The highest observed T_h may be affected by the tendency of calcite to leak fluid or stretch during deformation, resulting in an unrepresentative vapor to fluid ratio in the inclusion and elevating calculated T_h above the actual value (e.g., Goldstein and Reynolds, 1994). Fluid inclusions in calcite are particularly susceptible to thermal stress or other changes post-trapping (Bourdet and Pironon, 2008). Due to the possibility of overestimating T_h from stretched or leaked inclusions, temperature estimates at the lower part of this range are preferred (Bodnar, 2003).

We rely on the lowest temperature fluid inclusion temperatures (T_{hyd}) for sample KO18 in interpreting the $\delta^{18}O_{PDB}$ results for all samples collected in this study (78.5 °C, Table 2). The result is within what has reported for calcite veins collected from the NAF elsewhere (70 °C–170 °C; Janssen et al., 2009), which lends confidence that the approach is appropriate.

The present-day geothermal gradient in north central Turkey estimated by a Curie-point depth of ~22 km is 26 °C/km (Ates et al., 2005; Aydın et al., 2005). Assuming a surface temperature of ~20 °C and a 78.5 °C formation temperature, this would give a depth of ~2.2 km for the formation of the KO18 calcite vein. The Cretaceous geotherm is unknown, but these constraints appear reasonable given that open-mode fractures can occur up to these depths in trans-tensional and extensional systems (Sibson, 1996). The open-mode nature of the fractures indicated by calcite textures also implies that they formed at depths shallow enough to allow for fluid pressures to sustain open voids. Using methods described in Steele-MacInnis et al. (2012), pressures of 117–432 bar (Table 1) are estimated when invoking assumed thermobaric gradients of either an open or closed system. Due to the small size of the vapor

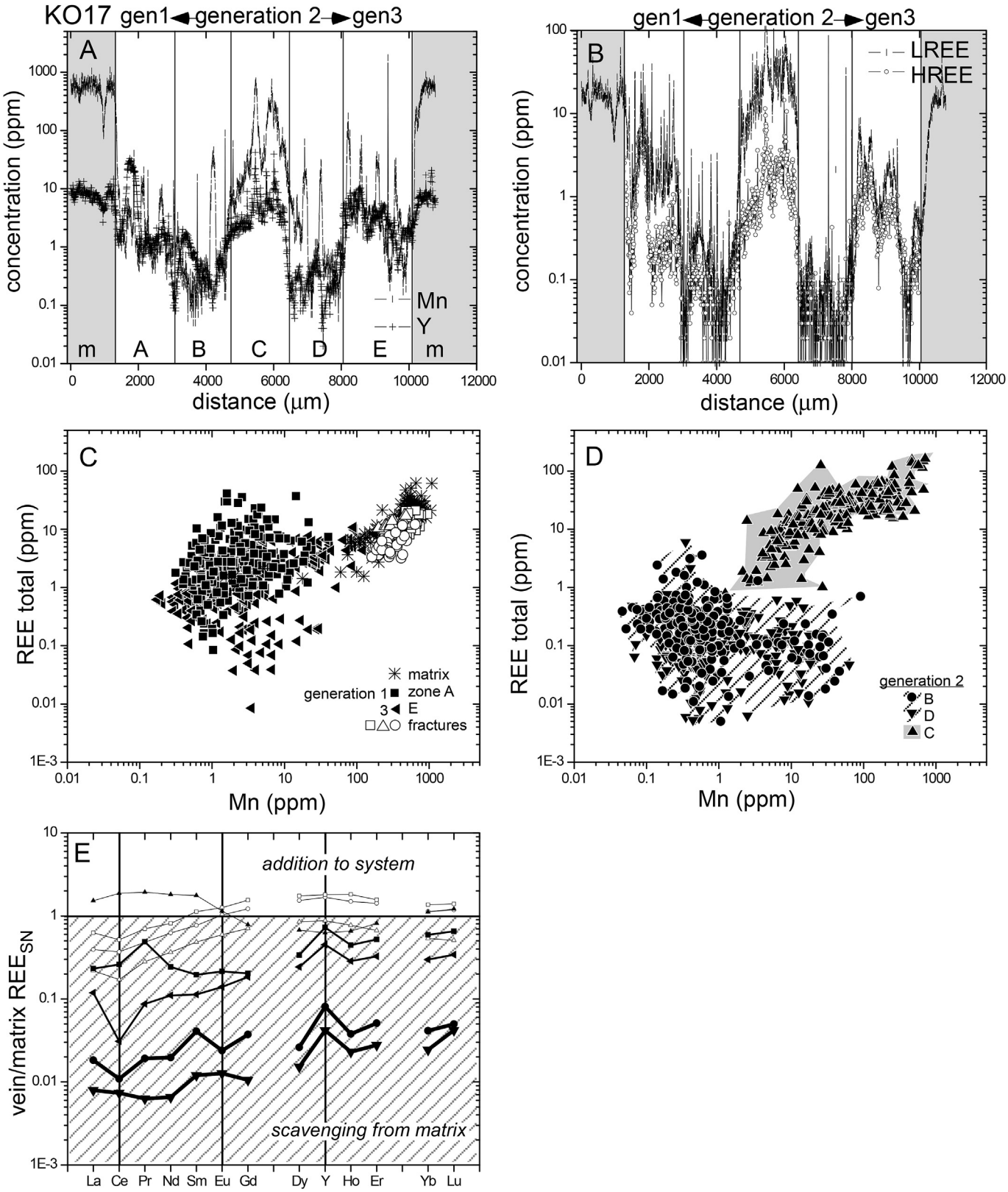

Fig. 13. LA-ICP-MS compositional transects across the vein in sample KO17 (Fig. 12) in (A) Mn and Y and (B) LREE and HREE. REE are La, Ce, Pr, Nd, Sm, Eu, Gd (LREE), Dy. Ho, Er, Yb, and Lu (HREE). Plots of Mn (ppm) vs. REE total (ppm) for KO17 analyses (C) of generations 1, 3, fractures, and the matrix, and (D) of generation 2 only. Some regions are shaded. (E) REE patterns of vein/matrix REE_{SN}. Area where vein/matrix REE_{SN} is ≤ 1 is suggested to be the result of interaction with the matrix. Region where REE_{SN} >1 suggests addition to the vein by sources external to the matrix.

Fig. 14. Composite of CL and reflected light images of sample KO17. The region is an offcut of the thin section in Fig. 12. The matrix calcite and generations (gen) 2 (zones B, C, and D) and 3 are labeled. Generation 1 was not observed in this offcut. Areas where SIMS $\delta^{18}O_{PDB}$ analyses were taken are identified by spots and transect numbers. Some values on fractures are indicated. See Supplementary data for analytical data.

bubbles, these inclusions likely did not form at higher pressure. In any case, the ~2.2 km depth is consistent with the range of baric estimates for the inclusions.

5.2.2. Fluid-rock interaction: stable isotopes

The IRMS $\delta^{13}C_{PDB}$ and $\delta^{18}O_{PDB}$ values of powdered samples are within the large range of what has been previously reported for calcite veins in rocks displaced by the NAF (Fig. 4) (Janssen et al., 1997, 2009) and is consistent with diagenetic calcite (e.g., Öztürk et al., 2002). The similarity of the matrix and vein in $\delta^{18}O_{PDB}$ obtained using IRMS (Table 1) suggest the fluid in which the vein precipitated was buffered by surrounding rock (Gray et al., 1991; Marquer and Burkhard, 1992; Muchez et al., 1995). Matrix-vein pairs show differences in $\delta^{18}O_{PDB}$ that range from 0.4 to 2.3‰ and in $\delta^{13}C_{PDB}$ from −0.9 to 4.6‰, suggesting most are consistent with a closed fluid system. Most samples have matrix IRMS $\delta^{18}O_{PDB}$ values that are greater than vein, with the exception of travertine sample KO16 where the matrix is 2.1‰ lower than the vein.

SIMS $\delta^{18}O_{PDB}$ data can be used to explore the nature of matrix buffering as some vein SIMS analyses differ significantly from the matrix IRMS values (Figs. 8, 11 and 15). For example, in sample KO16, the rock matrix IRMS $\delta^{18}O_{PDB}$ is −10.8‰, yet SIMS vein analyses fluctuate between from −7.4 ± 0.1‰ to −13.6 ± 0.1‰, with this lowest value is adjacent to the matrix (Fig. 11). In sample KO17,

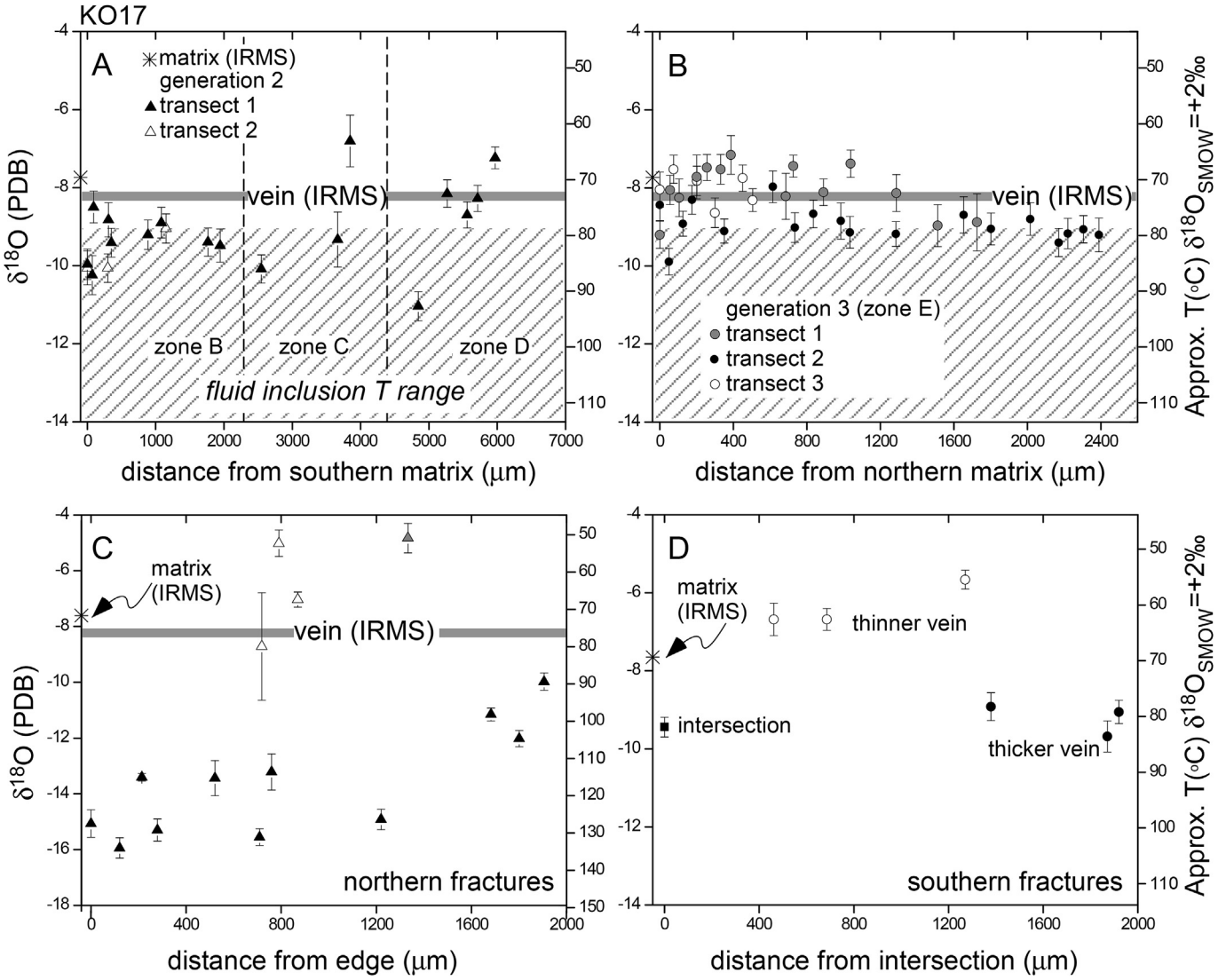

Fig. 15. SIMS $\delta^{18}O_{PDB}$ values across (A) generation 2 (B) generation 3, (C) northern fractures, and (D) southern fractures in sample KO17. The SIMS $\delta^{18}O_{PDB}$ values are translated into approximate temperatures using the equation of Hays and Grossman (1991) and assuming interacting fluids with $\delta^{18}O_{SMOW}$ of +2‰. See Fig. 14 for spot locations and Supplementary data for analytical data. In panels (A), (B), and (C) zones and the average $\delta^{18}O_{PDB}$ values for the vein obtained using IRMS are indicted. The matrix $\delta^{18}O_{PDB}$ is shown on each panel.

the matrix IRMS $\delta^{18}O_{PDB}$ is −7.8‰, and SIMS $\delta^{18}O_{PDB}$ of veins within the sample range from −15.9‰ to −4.8‰ (Fig. 15). In sample KO18, the rock matrix IRMS $\delta^{18}O_{PDB}$ value is −7.2‰ and a smaller fracture averages −7.8 ± 0.3‰ (Fig. 8). However, analyses across the thicker vein in this sample decrease from −8.4 ± 0.1‰ to −11.9 ± 0.8‰ within 200 μm of the wall rock (Fig. 8). These observations suggest that the extent of matrix/fluid buffering may be overestimated if only the IRMS $\delta^{18}O_{PDB}$ data from matrix/vein pairs are considered. Overall, at the high spatial resolution afforded by the SIMS analyses, we advocate the veins record limited rock buffering.

The $\delta^{18}O_{PDB}$ data from sample KO18 can be translated to temperatures assuming different values of interacting fluids (e.g., O'Neil et al., 1969; Friedman et al., 1977; Hays and Grossman, 1991; Morad et al., 2010; Vincent et al., 2007). Plotting these values on a fractionation diagram using $\delta^{18}O_{PDB}$ of calcite and various $\delta^{18}O_{SMOW}$ of possible parent fluids (Fig. 16) (e.g., Vincent et al., 2007) indicates that $\delta^{18}O_{SMOW\text{-}fluid}$ >+1‰ is required to reproduce the fluid inclusion temperatures found in the sample. Although Sea of Marmara bottom waters have $\delta^{18}O_{SMOW\text{-}fluid}$ of +1.58‰ (Rank et al., 1999; Crémiére et al., 2012), present-day values of water from nearby NAF geothermal fields (Gözlek site, −12.8 ± 0.6‰ to −10.0 ± 0.5‰; Suer et al., 2008) and present-day $\delta^{18}O_{SMOW}$ of meteoric water and groundwater in the sampling region (−9.5‰ to −13‰, Suer et al., 2008; Schemmel et al., 2013) are far lower. The value of $\delta^{18}O_{SMOW\text{-}fluid}$ of >+1‰ is more consistent with Cretaceous brines (+2‰, Morad et al., 2010; Zeebe, 2001), and provides a best fit, making a number of assumptions. These include: sample KO18 fluid inclusion temperatures can be applied to all samples and the fluids are present in excess and retain original isotopic compositions. Limited buffering is suggested by the high-resolution gradients in SIMS $\delta^{18}O_{PDB}$ data across the calcite veins. Note that the $\delta^{18}O_{SMOW}$ estimates for source water are not high enough to represent pure metamorphic or mantle origin, which is generally >+5‰ (Rollinson, 2014). Using these values in connection with the $\delta^{18}O_{PDB}$ calcite veins leads to unrealistic thermal conditions for mineralization.

Measurements of fine-scale variations in $\delta^{18}O_{PDB}$ across the veins show differences between individual spots <50 μm apart are

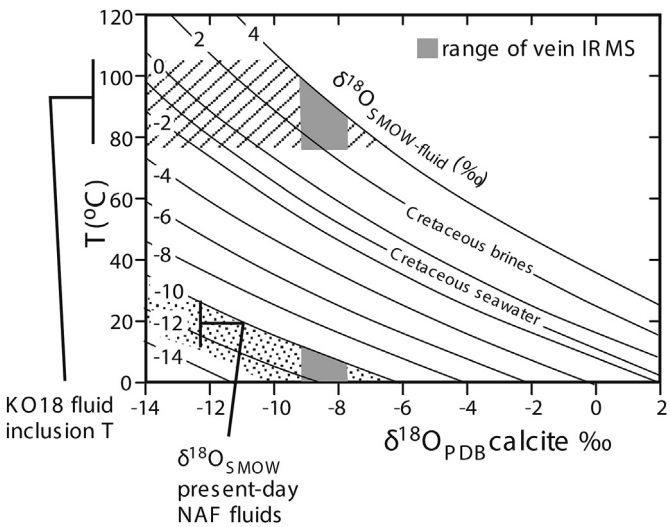

Fig. 16. Fractionation diagram between the $\delta^{18}O_{PDB}$ of calcite veins, the $\delta^{18}O_{SMOW\text{-}fluid}$ of its parent solutions, and its temperatures of precipitation (°C) after Vincent et al. (2007). Curves constructed with the equation of $10^3 \ln\alpha_{calcite\text{-}water} = 2.78 \times 10^6/T^2 - 2.89$ where $\alpha_{calcite\text{-}water}$ is the fractionation coefficient and T is the temperature in K (O'Neil et al., 1969). Regions of $\delta^{18}O_{PDB}$ of calcite veins obtained using IRMS are shaded. Also plotted is the range of fluid inclusion temperatures (78.5 °C–105.2 °C) and $\delta^{18}O_{PDB}$ of present-NAF geothermal waters (Gözlek site, $\delta^{18}O_{SMOW\text{-}fluid}$ of = −12.8 ± 0.6‰ to −10.0 ± 0.5‰; Suer et al., 2008). Lines of $\delta^{18}O_{SMOW\text{-}fluid}$ of Cretaceous carbonates and brines also indicated (after Morad et al., 2010; Grossman, 2012).

resolvable within the experimental error (±0.3‰, ±2σ) (Figs. 8, 11 and 15). Transects across veins perpendicular to the matrix in all samples (Figs. 8, 11 and 15) increase in $\delta^{18}O_{PDB}$ towards the vein centers, consistent with a temperature decrease, assuming a single fluid source. The observed thermal gradients (15.4 °C/mm in sample KO16 to 26 °C/mm in sample KO18 transect 1) are reasonable. Alternatively, assuming a single temperature for vein formation, changes in $\delta^{18}O_{PDB}$ values may be the result in changes of the $\delta^{18}O_{SMOW\text{-}fluid}$. Geochemical data suggests that the majority of zones within the veins show trends expected with single fluid, thus we prefer the interpretation that $\delta^{18}O_{PDB}$ reflects thermal changes.

Analyses of smaller fracture zones in sample KO17 have $\delta^{18}O_{PDB}$ that differ significantly from its larger vein calcite, suggesting that multiple events could be recorded or rock buffering affect these values (Fig. 15). Fluid inclusion data in sample KO18 shows extreme differences in temperature of up to 20 °C in adjacent inclusions (Table 2, Fig. 5). Although this is likely the result of analytical difficulties associated with these measurements, some of the isotopic results are consistent with extreme temperature differences in short proximity to each other. Two spots in sample KO18 located along the portion of transect 1 near the matrix within 40 μm yield $\delta^{18}O_{PDB}$ of −11.9 ± 0.8‰ and −9.4 ± 0.2‰ (T of 99.5 °C to 81.0 °C assuming $\delta^{18}O_{SMOW\text{-}fluid}$ of +2‰ and equation of Hays and Grossman, 1991) (Fig. 8). At the end of this transect, spots located 124 μm apart yield $\delta^{18}O_{PDB}$ of −11.2 ± 0.2‰ and −7.0 ± 0.2‰ (T of 94.4 °C to 64.9 °C, respectively). The former analyses samples a calcite grain with dark CL, whereas the latter analyses are located on a region of dark and bright CL, respectively. The results suggest that this portion of the calcite vein may record secondary alteration.

The IRMS $\delta^{13}C_{PDB}$ values for the calcite veins range from 0‰ in sample KO18 to −7.4‰ in sample KO16 (Table 1, Fig. 4). The $\delta^{13}C_{PDB}$ value of 0‰ in sample KO18 indicates a carbonate CO_2 source, likely inherited from the surrounding material. Organic carbon can affect the fluid chemistry to lower $\delta^{13}C_{PDB}$ values (Sharp, 2007). Sample KO17 has visible organic material (Fig. 3E). Differential incorporation of organic carbon would explain the 7‰ range in $\delta^{13}C_{PDB}$ across all samples. Although mantle-derived carbon with $\delta^{13}C_{PDB}$ (−5‰ to −8‰, Javoy et al., 1986) could result in similar observations, introduction of mantle material would likely also produce significant differences in the calcite $\delta^{18}O_{PDB}$, which is not observed.

5.2.3. Source of elements

The trace elements patterns of vein calcite in limestone assemblages has been suggested to reflect primarily the composition of the fluid in which they are in equilibrium (Barker and Cox, 2011; Bons et al., 2012). The majority of the REE + Y patterns for sampled segments of matrix and calcite veins exhibit negative Ce anomalies and positive Y anomalies (Fig. 7). Negative anomalies for Ce occur due to its tetravalent state (e.g., Smedley, 1991; Bau and Dulski, 1995; Bao et al., 2008; Nuriel et al., 2012a,b). This form of Ce^{4+} is highly insoluble in oxidizing conditions, correlating to low concentrations in fluids with neutral to high pH. A negative Ce anomaly is common in seawater as a result of oxidative absorption of Ce^{4+} onto Fe/Mn-oxyhydroxides. Carbonates formed from seawater, such as the limestones in this study, are predicted to inherit negative Ce anomalies from their waters of formation (Nuriel et al., 2012a).

The matrix in sample KO16 is the exception in that it does not show a Ce anomaly, but instead is the only region analyzed to have a positive Eu anomaly. Eu can become divalent under reducing conditions and thus become mobile in groundwater from which the calcite precipitated (Lee et al., 2003; Lavrushin et al., 2006). The positive Eu anomaly in this rock is consistent with textural observations that the rock is a travertine. Other sources for the Eu anomaly could be enrichment in Eu via preferential dissolution of plagioclase, clay minerals, or chlorite (Lee et al., 2003).

Similar to Ce, Y can be fractionated from Ho by redox conditions created in the presence of Fe/Mn-oxyhydroxides (e.g. Bau and Dulski, 1995; Bau et al., 1997, 2014). Unlike Ce, this process results in a positive anomaly due to the higher reactivity of Ho. This process can result in $Y_{CN}/Ho_{CN} > 28$ (value of bulk earth composition derived from chondritic meteorite; e.g., Tanaka et al., 2008). We anticipate that transects across vein calcite should increase in Ce and Y anomalies and decrease in REE with increasing distance from the matrix. This trend should occur due to interaction with the rock during crystallization of the vein calcite (e.g., Pili et al., 2002). Sample KO16 decreases in REE across the vein and increases in the magnitude of the Y anomaly (Fig. 7C and D, Fig. 10D). However, trends in Ce are interrupted when the transect reaches zone D. This zone fails to show a Ce anomaly, which suggests fluids that worked to develop this portion of the vein had a composition that differs from the majority of the vein. Samples KO17 and KO18 likewise decrease in REE from the matrix towards zone C and shows expected trends in Y and Ce anomalies (Fig. 7). However, the trend is interrupted in zone C in both rocks. This zone contains REE contents and chondrite- and shale-normalized enrichments greater than that of the matrix, likely related to the presence of Fe/Mn-oxides. The observed REE trends may be the result of receiving elements derived from the matrix (Figs. 6D and 13E). In sample KO17, REE patterns of smaller fractures in this rock closely resemble the matrix.

The process of vein formation can be further informed by CL, which activates primarily due to the presence of REE and Mn in carbonates (Richter et al., 2003). Each zone analyzed in the calcite veins define distinct Mn/REE ratios and trends (Figs. 6, 10 and 13). In sample KO16, zones A and B increase in REE with similar Mn contents as the matrix, but zones C, D, and E decrease in REE and Mn. Sample KO18 shows an opposite trend with increasing distance from the matrix, and sample KO17 matrix and smaller factures have

similar Mn/REE.

6. Tectonic implications

Although collected adjacent to the NAF system, larger calcite veins analyzed in this study suggest crystallization during process unrelated to movement along the structure. The formations from which the rocks were collected are known to have experienced a multistage tectonic history subsequent to their formation in the Liassic to mid-Cretaceous (Bektaş et al., 2001; Herece and Akay, 2003; Yilmaz, 2006; Cengiz Cinku, 2011). The unit records extensional, rift-related events during the Late Barremian to Early Aptian (e.g., Bektaş et al., 2001) and has been largely exposed during Pliocene-recent strike-slip tectonics (Barka et al., 2000).

The fluid inclusion portion of this study is consistent with the work of others that suggest the formation fluids of larger calcite veins experienced conditions of 83.8 ± 7.3 °C (T_h) to 91.4 ± 8.2 °C (T_{hyd}). The T_{hyd} conditions are used to identify possible $\delta^{18}O_{SMOW\text{-}fluid}$ compositions that worked to develop the $\delta^{18}O_{PDB}$ values of the veins. The geochemical evidence suggests vein formation during diagenesis with a Cretaceous fluid source, as opposed to present-day geothermal or meteoric fluids. The presence of smaller calcite fracture fill with significantly different $\delta^{18}O_{PDB}$ values than the larger veins in sample KO17 (Fig. 15) indicates the potential for smaller veins to experience matrix-vein buffering. All fractures yield values that yield unrealistic temperatures when paired with $\delta^{18}O_{SMOW}$ of present-day meteoric and hydrothermal fluids.

The formation of the calcite veins analyzed in this study at depths of ~2.2 km is reasonable (e.g., Sample, 2010; Holdsworth et al., 2011; Ferrill et al., 2014) as are the thermal gradients that the veins record during crystallization. According to the Republic of Turkey Prime Ministry Disaster and Emergency Management Authority database, most of the earthquakes that occurred in the region from 1900-2017 in the field area (Fig. 1) have epicenters at 1–40 km depth, with most occurring >10 km. We find that the fractured limestones we collected along the Niksar basin provide no evidence of a deep-seated crustal fluid source, however, this may be an outcome of the sampling strategy and the limited number of analyses. Seismic pumping, where episodic injections of hot fluids with dissolved gases and calcite occur upwards from deeper structural levels and reprecipitate calcite in permeable zones due to earthquake motion (e.g., Wood and Boles, 1991), is not observed in the samples we collected. The hydraulic regime of the fault system is strongly influenced by a number of factors, including the composition of the fluid, pCO_2, and the nature of the fracture and fault network (e.g., Frima et al., 2005). The Marmara Main Fault (Fig. 1), the splay of the NAF within the Sea of Marmara, displays ample evidence exists for deep-seated crustal fluids venting through the NAF (Fig. 1) (e.g., Burnard et al., 2012; Tryon et al., 2012). Thus, this work indicates heterogeneity fluid motion within the NAF along strike. Fluids play a role in influencing deeper parts of the NAF, but we find evidence for these deeper fluids in calcite veins analyzed in this portion of the structure. The approach described in this paper is of value in terms of seeking to understand the role and nature of the structural permeability of this portion of the NAF, or other fault systems that displace carbonate assemblages.

Acknowledgements

We appreciate constructive discussions with Peter Eichhubl (UT Austin, Bureau of Economic Geology) and Jaime Barnes (UT Austin, Dept. of Geological Sciences), and analytical assistance by Ming-Chang Liu in the UCLA SIMS lab. The ion microprobe facility at UCLA is partly supported by a grant from the Instrumentation and Facilities Program, Division of Earth Sciences, National Science Foundation Award #1339051. The project was funded by the University of Texas System of Austin Vice President of Research Office and the Jackson School of Geosciences. We appreciate a constructive reviews by Nicolas Beaudoin, Philippe Boulvais, and an anonymous reviewer and editorial handling by Ian Alsop.

Appendix A. Supplementary data

Supplementary data related to this article can be found at http://dx.doi.org/10.1016/j.jsg.2017.06.004.

References

Adiyaman, O., Chorowicz, J., Arnaud, O.N., Gundogdu, M.N., Gourgaud, A., 2001. Late Cenozoic tectonics and volcanism along the North Anatolian Fault; new structural and geochemical data. Tectonophysics 338, 135–165.
Aktimur, H.T., Yurdakul, M.E., Urgun, B.M., Ates, S., Teoman, S., 1990. Tokat- D23 Paftasi, 1:100,000 olcekli. Turkiye Jeoloji Haritalari Serisi. Maden Tetkik ve Arama Genel Mudurlugu, Ankara (Geological map of the Tokat Massif, in Turkish).
Akyuz, H.S., Hartleb, R., Barka, A.A., Altunel, E., Sunal, G., Meyer, B., Armijo, R., 2002. Surface rupture and slip distribution of the 12 November 1999 Duzce earthquake (M 7.1), North Anatolian fault, Bolu, Turkey. Bull. Seismol. Soc. Am. 92, 61–66.
Ambraseys, N.N., Jackson, J.A., 1998. Faulting associated with historical and recent earthquakes in the eastern Mediterranean region. Geophys. J. Int. 133, 390–406.
Ates, A., Bilim, F., Buyuksarac, A., 2005. Curie point depth investigation of Central Anatolia, Turkey. Pure Appl. Geophys. 162, 357–371.
Aydın, İ., Karat, H.İ., Koçak, A., 2005. Curie-point depth map of Turkey. Geophys. J. Int. 162, 633–640.
Barka, A.A., 1992. The north Anatolian fault zone. Ann. Tect. 6, 164–195.
Barka, A.A., 1996. Slip distribution along the North Anatolian Fault associated with large earthquakes of the period 1939 to 1967. Bull. Seismol. Soc. Am. 86, 1238–1254.
Barka, A.A., Akyüz, H.S., Cohen, H.A., Watchorn, F., 2000. Tectonic evolution of the Niksar and Taşova-Erbaa pull-apart basins, North Anatolian fault zone: their significance for the motion of the Anatolian block. Tectonophysics 322, 243–264.
Barka, A.A., Hancock, P.L., 1984. Neotectonic deformation patterns in the convex-northwards arc of the North Anatolian fault zone. Geol. Soc. Lond. Special Publ. 17, 763–774.
Barker, S.L., Cox, S.F., 2011. Oscillatory zoning and trace element incorporation in hydrothermal minerals; insights from calcite growth experiments. Geofluids 11, 48–56.
Bao, S., Zhou, H., Peng, X., Ji, F., Yao, H., 2008. Geochemistry of REE and yttrium in hydrothermal fluids from the Endeavour segment, Juan de Fuca Ridge. Geochem. J. 42, 359–370.
Bau, M., Dulski, P., 1995. Comparative study of yttrium and rare-earth element behaviours in fluorine-rich hydrothermal fluids. Contrib. Mineral. Petrol. 119, 213–223.
Bau, M., Moeller, P., Dulski, P., 1997. Yttrium and lanthanides in eastern Mediterranean seawater and their fractionation during redox-cycling. Mar. Chem. 56, 123–131.
Bau, M., Schmidt, K., Koschinsky, A., Hein, J., Kuhn, T., Usui, A., 2014. Discriminating between different genetic types of marine ferro-manganese crusts and nodules based on rare earth elements and yttrium. Chem. Geol. 381, 1–9.
Bektaş, O., Capkinoglu, S., Akdag, K., 2001. Successive extensional tectonic regimes during the Mesozoic as evidenced by neptunian dikes in the Pontide magmatic arc, Northeast Turkey. Int. Geol. Rev. 43, 840–849.
Bodnar, R.J., 2003. Re-equilibration of fluid inclusions. In: Samson, I., Anderson, A., Marshall, D. (Eds.), Fluid Inclusions: Analysis and Interpretation, vol. 32. Mineralogical Association of Canada Short Course, pp. 213–231.
Bons, P.D., Elburg, M.A., Gomez-Rivas, E., 2012. A review of the formation of tectonic veins and their microstructures. J. Struct. Geol. 43, 33–62.
Bourdet, J., Pironon, J., 2008. Strain response and re-equilibration of CH_4-rich synthetic aqueous fluid inclusions in calcite during pressure drops. Geochim. Cosmochim. Acta 72, 2946–2959.
Bredehoeft, J.D., Ingebritsen, S.E., 1990. Degassing of Carbon Dioxide as a Possible Source of High Pore Pressures in the Crust, the Role of Fluids in Crustal Processes. National Academy Press, Washington, DC, pp. 158–164.
Burnard, P., Bourlange, S., Henry, P., Geli, L., Tryon, M.D., Natalin, B., Şengör, A.M.C., Özeren, M.S., Çagatay, M.N., 2012. Constraints on fluid origins and migration velocities along the Marmara Main Fault (Sea of Marmara, Turkey) using helium isotopes. Earth Planet. Sci. Lett. 341–344, 68–78.
Bussolotto, M., Benedicto, A., Moen-Maurel, L., Invernizzi, C., 2015. Fault deformation mechanisms and fault rocks in micritic limestones; examples from Corinth Rift normal faults. J. Struct. Geol. 77, 191–212.
Byerlee, J.D., 1993. Model for episodic flow of high-pressure water in fault zones before earthquakes. Geology 21, 303–306.

Caine, J.S., Evans, J.P., Forster, C.B., 1996. Fault zone architecture and permeability structure. Geology 24, 1025–1028.
Catlos, E.J., Huber, K., Shin, T.A., 2013. Geochemistry and geochronology of meta-igneous rocks from the Tokat Massif, north-central Turkey; implications for Tethyan reconstructions. Int. J. Earth Sci. Geol. Rundschau 102, 2175–2198.
Cengiz Cinku, M., 2011. Paleogeographic evidence on the Jurassic tectonic history of the Pontides; new paleomagnetic data from the Sakarya continent and eastern Pontides. Int. J. Earth Sci. Geol. Rundschau 100, 1633–1645.
Chiodini, G., Cardellini, C., Amato, A., Boschi, E., Caliro, S., Frondini, F., Ventura, G., 2004. Carbon dioxide Earth degassing and seismogenesis in central and southern Italy. Geophys. Res. Lett. 31 http://dx.doi.org/10.1029/2004GL019480.
Coplen, T.B., 1994. Reporting of stable hydrogen, carbon, and oxygen isotopic abundances. Pure Appl. Chem. 66, 273–276.
Crémiére, A., Pierre, C., Blanc-Valleron, M.-M., Zitter, T., Çağatay, M.N., Henry, P., 2012. Methane-derived authigenic carbonates along the north Anatolian Fault system in the Sea of Marmara (Turkey). Deep-Sea Res. Part I Oceanogr. Res. Pap. 66, 114–130.
Dabi, G., Bajnóczi, B., Schubert, F., Tóth, M., T.M., 2013. The origin and role of a calcite-filled microcrack generation in a metamorphic crystalline complex: the characterization of a fossilised seismic permeability system. Tectonophysics 608, 792–803.
D'Alessandro, W., Giammanco, S., Bellomo, S., Parello, F., 2007. Geochemistry and mineralogy of travertine deposits of the SW flank of Mt. Etna (Italy): relationships with past volcanic and degassing activity. J. Volcanol. Geotherm. Res. 165, 64–70.
De Leeuw, G.A.M., Hilton, D.R., Güleç, N., Mutlu, H., 2010. Regional and temporal variations in $CO_2/^3He$, $^3He/^4He$ and $\delta^{13}C$ along the north Anatolian fault zone, Turkey. Appl. Geochem. 25, 524–539.
Demir, G., Aytekin, M., Akgun, A., 2015. Landslide susceptibility mapping by frequency ratio and logistic regression methods: an example from Niksar-Resadiye (Tokat, Turkey). Arab. J. Geosci. 8, 1801–1812.
Doğan, T., Sumino, H., Nagao, K., Notsu, K., Tuncer, M.K., Celik, C., 2009. Adjacent releases of mantle helium and soil CO_2 from active faults: observations from the Marmara region of the North Anatolian Fault zone, Turkey. Geochem. Geophys. Geosys. 10, Q11009. http://dx.doi.org/10.1029/2009GC002745.
El Desouky, H., Soete, J., Claes, H., Ozkul, M., Vanhaecke, F., Swennen, R., 2015. Novel applications of fluid inclusions and isotope geochemistry in unravelling the genesis of fossil travertine systems. Sedimentology 62, 27–56.
Emre, Ö., Duman, T.Y., Kondo, H., Özalp, S., Elmacı, H., 2012. 1:250 000 Scale Active Fault Map Series of Turkey, Tokat (NK 37-13) Quadrangle. Serial Number: 35. General Directorate of Mineral Research and Exploration, Ankara, Turkey.
Erol, G., Topal, T., 2013. GIS-based microzonation of the Niksar settlement area for the purpose of urban planning (Tokat, Turkey). Environ. Earth Sci. 68, 2065–2084.
Erturac, M.K., Tüysüz, O., 2012. Kinematics and basin formation along the Ezinepazar Sungurlu fault zone, NE Anatolia, Turkey. Turk. J. Earth Sci. 21, 497–520.
Ferrill, D.A., McGinnis, R.N., Morris, A.P., Smart, K.J., Sickmann, Z.T., Bentz, M., Evans, M.A., 2014. Control of mechanical stratigraphy on bed-restricted jointing and normal faulting; Eagle Ford Formation, south-central Texas. Am. Assoc. Pet. Geol. Bull. 98, 2477–2506.
Fichtner, A., Saygin, E., Taymaz, T., Cupillard, P., Capdeville, Y., Trampert, J., 2013. The deep structure of the North Anatolian fault zone. Earth Planet. Sci. Lett. 373, 109–117.
Friedman, I., O'Neil, J.R., Fleischer, M.E., 1977. Compilation of Stable Isotope Fractionation Factors of Geochemical Interest. U.S. Geological Survey Professional Paper 440-KK, 11pp.
Frima, C., Moretti, I., Brosse, E., Quattrocchi, F., Pizzino, L., 2005. Can diagenetic processes influence the short term hydraulic behaviour evolution of a fault? Oil Gas Sci. Technol. 60, 213–230.
Gray, D.R., Gregory, R.T., Durney, D.W., 1991. Rock-buffered fluid-rock interaction in deformed quartz-rich turbidite sequences, eastern Australia. J. Geophys. Res. 96, 19681–19704.
Gokten, Y.E., Kelling, G., Meydan, M., 2013. The kinematic significance of rotation-related deformation features in a fault-defined wedge associated with the North Anatolian Fault, central Turkey. J. Geodyn. 65, 228–243.
Goldstein, R.H., Reynolds, T.J., 1994. Systematics of fluid inclusions in diagenetic minerals. Soc. Sediment. Geol. (SEPM) Short Course 31, 199 pp.
Grossman, E.L., 2012. Applying oxygen isotope paleothermometry in deep time. In: Ivany, L.C., Huber, B.T. (Eds.), Reconstructing Earth's Deep-time Climate – the State of the Art in 2012, vol. 18. Paleontological Society Papers, pp. 39–67.
Gürsoy, H., Tatar, O., Akpinar, Z., Polat, A., Mesci, L., Tuncer, D., 2013. New observations on the 1939 Erzincan earthquake surface rupture on the Kelkit valley segment of the north Anatolian fault zone, Turkey. J. Geodyn. 65, 259–271.
Haskin, M.A., Haskin, L.A., 1966. Rare earths in European shales; a redetermination. Science 154, 507–509.
Hays, P.D., Grossman, E.L., 1991. Oxygen isotopes in meteoric calcite cements as indicators of continental paleoclimate. Geology 19, 441–444.
Hempton, M.R., Dunne, L.A., 1984. Sedimentation in pull-apart basins; active examples in eastern Turkey. J. Geol. 92, 513–530.
Herece, E., Akay, E., 2003. In: Kaf Boyu Jeoloji Haritasi - (Destek-Niksar) (Geologic Map along NAF (Destek-Niksar)) 1:100,000. Atlas of North Anatolian Fault (NAF), vol. 61. General Directorate of Mineral Research and Exploration, Special Publication series-2, Ankara, p. 13.
Hilgers, C., Urai, J.L., 2002. Microstructural observations on natural syntectonic fibrous veins; implications for the growth process. Tectonophysics 352, 257–274.
Holdsworth, R.E., van Diggelen, E.E., Spiers, C.J., de Bresser, J.P., Walker, R.J., Bowen, L., 2011. Fault rocks from the SAFOD core samples; implications for weakening at shallow depths along the San Andreas Fault, California. J. Struct. Geol. 33, 132–144.
Hoefs, J., 1997. Stable Isotope Geochemistry. Springer-Verlag, Berlin, Germany.
Hubert-Ferrari, A., Armijo, R., King, G., Meyer, B., Barka, A., 2002. Morphology, displacement, and slip rates along the north Anatolian fault, Turkey. J. Geophys. Res. 107, 1–33.
Hudson, J.D., 1977. Stable isotopes and limestone lithification. J. Geol. Soc. Lond. 133, 637–660.
Janssen, C., Bohnhoff, M., Vapnik, Y., Gorgun, E., Bulut, F., Plessen, B., Dresen, G., 2009. Tectonic evolution of the Ganos segment of the north Anatolian fault (NW Turkey). J. Struct. Geol. 31, 11–28.
Janssen, C., Michel, G.W., Bau, M., Lueders, V., Muehle, K., 1997. The North Anatolian fault zone and the role of fluids in seismogenic deformation. J. Geol. 105, 387–403.
Javoy, M., Pineau, F., Delorme, H., 1986. Carbon and nitrogen isotopes in the mantle. Chem. Geol. 57, 41–62.
Kenis, I., Muchez, P., Sintubin, M., Mansy, J.L., Lacquement, F., 2000. The use of a combined structural, stable isotope and fluid inclusion study to constrain the kinematic history at the northern Variscan front zone (Bettrechies, northern France). J. Struct. Geol. 22, 589–602.
Lavrushin, V.Y., Kuleshov, V.N., Kikvadze, O.E., 2006. Travertines of the northern caucasus. Lithol. Miner. Resour. 41, 137–164.
Lee, S-G., Lee, D-H., Kim, Y., Chae, B-G., Kim, W-Y., Woo, N-C., 2003. Rare earth elements as indicators of groundwater environment changes in a fractured rock system; evidence from fracture-filling calcite. Appl. Geochem. 18, 135–143.
Mann, P., Hempton, M.R., Bradley, D.C., Burke, K., 1983. Development of pull-apart basins. J. Geol. 91, 529–554.
Marquer, D., Burkhard, M., 1992. Fluid circulation, progressive deformation and mass-transfer processes in the upper crust. The example of basement-cover relationships in the External Crystalline Massifs, Switzerland. J. Struct. Geol. 14, 1047–1057.
Miller, S.A., Collettini, C., Chiaraluce, L., Cocco, M., Barchi, M., Kaus, B.J.P., 2004. Aftershocks driven by a high-pressure CO_2 source at depth. Nature 427, 724–727.
Moix, P., Beccaletto, L., Kozur, H.W., Hochard, C., Rosselet, F., Stampfli, G.M., 2008. A new classification of the Turkish terranes and sutures and its implication for the paleotectonic history of the region. Tectonophysics 451, 7–39.
Moore, D., Lockner, D.A., Ito, H., Ikeda, R., 2000. Carbonate mineralization sequence and the earthquake history of the Nojima fault zone, Japan. Eos Trans. AGU 81 (48). Fall Meet. Suppl., Abstract T52E-02.
Morad, S., Al-Aasm, I.S., Sirat, M., Sattar, M.M., 2010. Vein calcite in Cretaceous carbonate reservoirs of Abu Dhabi; record of origin of fluids and diagenetic conditions. J. Geochem. Explor. 106, 156–170.
Muchez, P., Slobodnik, M., Viaene, W.A., Keppens, E., 1995. Geochemical constraints on the origin and migration of palaeofluids at the northern margin of the Variscan foreland, southern Belgium. Sediment. Geol. 96, 191–200.
Nuriel, P., Rosenbaum, G., Zhao, J.X., Feng, Y., Golding, S.D., Villemant, B., Weinberger, R., 2012b. U-Th dating of striated fault planes. Geology 40, 647–650.
Nuriel, P., Weinberger, R., Rosenbaum, G., Golding, S.D., Zhao, J.X., Uysal, I.T., Gross, M.R., 2012a. Timing and mechanism of late-Pleistocene calcite vein formation across the Dead Sea Fault Zone, northern Israel. J. Struct. Geol. 36, 43–54.
Olierook, H.H., Timms, N.E., Hamilton, P.J., 2014. Mechanisms for permeability modification in the damage zone of a normal fault, northern Perth Basin, Western Australia. Mar. Pet. Geol. 50, 130–147.
O'Neil, J.R., Clayton, R.N., Mayeda, T.K., 1969. Oxygen isotope fractionation in divalent metal carbonates. J. Chem. Phys. 51, 5547–5558.
Ozden, S., Over, S., Unlunenc, U.C., 2002. Quaternary stress regime change along the eastern North Anatolian fault zone, Turkey. Int. Geol. Rev. 44, 1037–1052.
Öztürk, H., Hein, J.R., Hanilci, N., 2002. Genesis of the Dogankuzu and Mortas bauxite deposits, Taurides, Turkey; separation of Al, Fe, and Mn and implications for passive margin metallogeny. Econ. Geol. Bull. Soc. Econ. Geol. 97, 1063–1077.
Peacock, D.P., Anderson, M.W., 2012. The scaling of pull-aparts and implications for fluid flow in areas with strike-slip faults. J. Pet. Geol. 35, 389–399.
Pentecost, A., 2005. Travertine. Springer Verlag, Berlin, 446 pp.
Pili, E., Poitrasson, F., Gratier, J., 2002. Carbon-oxygen isotope and trace element constraints on how fluids percolate faulted limestones from the San Andreas fault system; partitioning of fluid sources and pathways. Chem. Geol. 190, 231–250.
Pili, E., Kennedy, B.M., Conrad, M.E., Gratier, J.P., 2011. Isotopic evidence for the infiltration of mantle and metamorphic CO_2 –H_2O fluids from below in faulted rocks from the San Andreas fault system. Chem. Geol. 281, 242–252.
Piper, D.Z., 2001. Marine chemistry of the Permian Phosphoria formation and basin, Southeast Idaho. Econ. Geol. Bull. Soc. Econ. Geol. 96, 599–620.
Piper, J.A., Gursoy, H., Tatar, O., Beck, M.E., Rao, A., Kocbulut, F., Mesci, B.L., 2010. Distributed neotectonic deformation in the Anatolides of Turkey; a palaeomagnetic analysis. Tectonophysics 488, 31–50.
Ran, G., Eyal, S., Yoseph, Y., Amir, S., Noam, W., 2014. The permeability of fault zones; a case study of the Dead Sea Rift (Middle East). Hydrogeol. J. 22, 425–440.
Ramsay, J.G., 1980. The crack–seal mechanism of rock deformation. Nature 284,

135–139.
Rank, D., Ozsoy, E., Salihoglu, I., 1999. Oxygen-18, deuterium and tritium in the Black Sea and the Sea of Marmara. J. Environ. Radioactiv. 43, 231–245.
Rice, J.R., 1992. Fault stress states, pore pressure distributions, and the weakness of the San Andreas Fault. Int. Geophys. 51, 475–503.
Richter, D.K., Gotte, T., Götze, J., Neuser, R.D., 2003. Progress in application of cathodoluminescence (CL) in sedimentary petrology. Mineral. Petrol. 79, 127–166.
Ritz, E., Pollard, D.D., Ferris, M., 2015. The influence of fault geometry on small strike-slip fault mechanics. J. Struct. Geol. 73, 49–63.
Roberts, G.P., 1994. Displacement localization and palaeo-seismicity of the rencurel thrust zone, French sub-alpine chains. J. Struct. Geol. 16, 633–646.
Rojay, B., 1995. Post-Triassic evolution of central Pontides; evidence from Amasya region, northern Anatolia. Geol. Romana 31, 329–350.
Rollinson, H.R., 2014. Using Geochemical Data: Evaluation, Presentation, Interpretation. Routledge, London, UK.
Sample, J.C., 2010. Stable isotope constraints on vein formation and fluid evolution along a recent thrust fault in the Cascadia accretionary wedge. Earth Planet. Sci. Lett. 293, 300–312.
Schemmel, F., Mikes, T., Rojay, B., Mulch, A., 2013. The impact of topography on isotopes in precipitation across the Central Anatolian Plateau (Turkey). Am. J. Sci. 313, 61–80.
Şengör, A.M.C., Gorur, N., Saroglu, F., 1985. Strike-slip faulting and related basin formation in zones of tectonic escape; Turkey as a case study. Special Publ. - Soc. Econ. Paleontol. Mineral. 37, 227–264.
Şengör, A.C., Tuysuz, O., Imren, C., Sakinc, M., Eyidogan, H., Gorur, N., Rangin, C., 2005. The North Anatolian fault; a new look. Annu. Rev. Earth Planet. Sci. 33, 37–112.
Sharp, Z., 2007. Principles of Stable Isotope Geochemistry. Pearson Education, Upper Saddle River, NJ.
Sibson, R.H., 1996. Structural permeability of fluid-driven fault-fracture meshes. J. Struct. Geol. 18, 1031–1042.
Sibson, R.H., Moore, J.M.M., Rankin, A.H., 1975. Seismic pumping—a hydrothermal fluid transport mechanism. J. Geol. Soc. 131, 653–659.
Smedley, P.L., 1991. The geochemistry of rare earth elements in groundwater from the Carnmenellis area, Southwest England. Geochim. Cosmochim. Acta 55, 2767–2779.
Steele-MacInnis, M., Lecumberri-Sanchez, P., Bodnar, R.J., 2012. HOKIEFLINCS_H2O NACL: a Microsoft Excel spreadsheet for interpreting microthermometric data from fluid inclusions based on the PVTX properties of H_2O-NaCl. Comput. Geosci. 49, 334–337.
Suer, S., Gulec, N., Mutlu, H., Hilton, D.R., Cifter, C., Sayin, M., 2008. Geochemical monitoring of geothermal waters (2002-2004) along the North Anatolian fault zone, Turkey; spatial and temporal variations and relationship to seismic activity. Pure Appl. Geophys. 165, 17–43.
Sun, S.S., McDonough, W.F., 1989. Chemical and isotopic systematics of oceanic basalts; implications for mantle composition and processes. Geol. Soc. Spec. Publ. 42, 313–345.
Tanaka, K., Takahashi, Y., Shimizu, H., 2008. Local structure of Y and Ho in calcite and its relevance to Y fractionation from Ho in partitioning between calcite and aqueous solution. Chem. Geol. 248, 104–113.
Tatar, O., Piper, J.D.A., Park, R.G., Gursoy, H., 1995. Palaeomagnetic study of block rotations in the Niksar overlap region of the north Anatolian fault zone, central Turkey. Tectonophysics 244, 251–266.
Tatar, O., Yurtmen, S., Temiz, H., Gursoy, H., Kocbulut, F., Mesci, B.L., Guezou, J.C., 2007. Intracontinental Quaternary volcanism in the Niksar pull-apart basin, North Anatolian fault zone, Turkey. Turk. J. Earth Sci. 16, 417–440.
Türkoğlu, E., Unsworth, M., Bulut, F., Çağlar, İ., 2015. Crustal structure of the north Anatolian and East Anatolian fault systems from magnetotelluric data. Phys. Earth Planet. Inter. 241, 1–14.
Tryon, M.D., Henry, P., Hilton, D.R., 2012. Quantifying submarine fluid seep activity along the north Anatolian fault zone in the Sea of Marmara. Mar. Geol. 315–318, 15–28.
Uysal, I.T., Feng, Y.X., Zhao, J.X., Bolhar, R., Işik, V., Baublys, K.A., Golding, S.D., 2011. Seismic cycles recorded in late Quaternary calcite veins: geochronological, geochemical and microstructural evidence. Earth Planet. Sci. Lett. 303, 84–96.
Uysal, I.T., Mutlu, H., Altunel, E., Karabacak, V., Golding, S.D., 2006. Clay mineralogical and isotopic (K-Ar, $\delta^{18}O$, δD) constraints on the evolution of the North Anatolian fault zone, Turkey. Earth Planet. Sci. Lett. 243, 181–194.
Verhaert, G., Muchez, P., Sintubin, M., Similox-Tohon, D., Vandycke, S., Waelkens, M., 2003. Reconstruction of neotectonic activity using carbonate precipitates: a case study from the northwestern extremity of the Isparta Angle (SW Turkey). J. Geochem. Explor. 78, 197–201.
Verhaert, G., Muchez, P., Sintubin, M., Similox-Tohon, D., Vandycke, S., Keppens, E., Richards, D.A., 2004. Origin of palaeofluids in a normal fault setting in the Aegean region. Geofluids 4, 300–314.
Vincent, B., Emmanuel, L., Houel, P., Loreau, J., 2007. Geodynamic control on carbonate diagenesis; petrographic and isotopic investigation of the Upper Jurassic formations of the Paris Basin (France). Sediment. Geol. 197, 267–289.
Wood, J.R., Boles, J.R., 1991. Evidence for episodic cementation and diagenetic recording of seismic pumping events, North Coles Levee, California, U.S.A. Appl. Geochem. 6, 509–521.
Yilmaz, A., Yilmaz, H., 2004. Geology and structural evolution of the Tokat massif (eastern Pontides, Turkey). Turk. J. Earth Sci. 13, 231–246.
Yilmaz, C., 2006. Platform-slope transition during rifting; the Mid-Cretaceous succession of the Amasya region (northern Anatolia), Turkey. J. Asian Earth Sci. 27, 194–206.
Yilmaz, Y., Serdar, H.S., Genc, C., Yigitbas, E., Gürer, Ö.F., Elmas, A., Gürpinar, O., 1997. The geology and evolution of the Tokat Massif, south-central Pontides, Turkey. Int. Geol. Rev. 39, 365–382.
Yoshioka, T., 1996. Evolution of fault geometry and development of strike-slip basins: comparative studies on the transform zones in Turkey and Japan. Isl. Arc 5, 407–419.
Zabci, C., Akyuz, H.S., Karabacak, V., Sancar, T., Altunel, E., Gursoy, H., Tatar, O., 2011. Palaeoearthquakes on the Kelkit valley segment of the north Anatolian fault, Turkey; implications for the north Anatolian fault, Turkey; implications for the surface rupture of the historical 17 August 1668 Anatolian earthquake. Turk. J. Earth Sci. 20, 411–427.
Zeebe, R.E., 2001. Seawater pH and isotopic paleotemperatures of Cretaceous oceans. Palaeogeogr. Palaeoclimatol. Palaeoecol. 170, 49–57.